TÉCNICO LISBOA

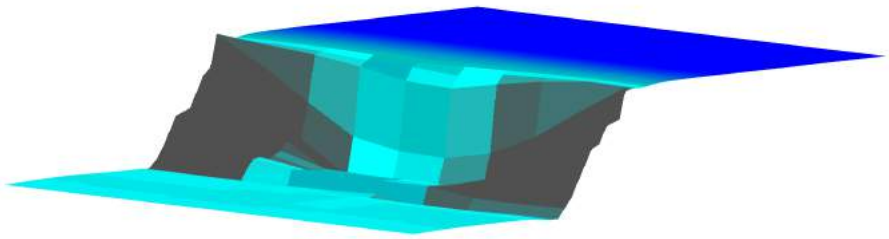

Numerical Modeling of Earth Dam Breaching by Overtopping

André Filipe Paulos Lopes

Thesis to obtain the Master of Science Degree in

Civil Engineering

Supervisor: Professor Rui Miguel Lage Ferreira
Supervisor: Professor Maria Rafaela Pinheiro Cardoso

Examination Committee

Chairperson:	Professor António Alexandre Trigo Teixeira
Supervisor:	Professor Rui Miguel Lage Ferreira
Member of the Committee:	Dr. Maria Teresa Fontelas dos Santos Viseu

November 2015

To my parents and brothers: António, Paula, Mara, Daniel e Lidía, Obrigado.

Acknowledgments

This dissertation was developed at Instituto Superior Técnico - Technical University of Lisbon, Portugal, under the guidance of Professors Rui M. L. Ferreira and Maria Rafaela Pinheiro Cardoso.

Part of the work was developed at LNEC, with the help of Jõao Santos, under the supervision of Eng. Silvia Rute Caleiro Amaral, Dr. Maria Teresa Viseu and assistance from Eng. Ricardo Jonatas from the Department of Hydraulics and Environment (DHA). The assistance and expertise from Professor Laura Caldeira and Eng. Joaquim Timóteo Silva from the Geotechnical Department (DG) were also of great importance towards making the experiments a success.

I am very grateful for the experience, and everything I have learned over the course of this work for that I want to express me gratitude to professor Rui Miguel Laje Ferreira, I hope i have reached your expectations, and I thank you for the push towards hydraulics.

To professor Maria Rafaela Cardoso, I thank you for all the patience and all the knowledge taught to me, I am still trying to catch up.

To everyone who I met while in my internship in LNEC, I thank you, to Silvia, Jõao, Ricardo, Nuno, Yury, André for the lessons i learned, for the companionship and hard work.

To my colleagues and friends, i have to say these have been a handful of memorable years and people, Afonso, João, André, Joana(s), Daniela, Elsa and Bruno, thank you for making my days amazing, thank you for the friendship and the laughs. João, Afonso and André notice! I have mentioned you and ”wash out” for any undesirable comments!

To my girlfriend, thank you for everything for sharing these almost 3 amazing years, and for the patience! All I can say is that i want more!

To my family, my father and mother, Antonio and Paula, there are no better parents in the world, you are the reason i am here today and I hope i can be as hardworking and as dedicated to my family as you are to me! To my brother and sisters, thank you for always putting up with me, for being there for me and for all we have lived together. To Lidia e leave a kiss right here for you to read.

Finally I would like to express my gratitude for two people who will not be able to read this, Mina and Tio Zé I still think about you everyday, i hope i can make you proud, and I wish you where here!

For any person I have not yet mentioned, I want to thank you.I could write a book with all of you and I am grateful for that!

Resumo

As barragens e reservatórios são fundamentais para o desenvolvimento socioeconómico de qualquer civilização porque providenciam água e energia. O aumento da pressão demográfica levou à necessidade de construir barragens para armazenamento de água, e portanto surgiram riscos de inundação nos vales de jusante. Roturas de barragem levam a perdas económicas severas e danos ambientais, havendo elevada probabilidade para perda de vidas humanas. Há múltiplas causas de rotura de barragens, sendo o galgamento e a erosão interna os mais comuns em barragens de aterro (ICOLD (2013)).

Um modelo numérico existente, STAV2D, foi adaptado para uma nova linguagem, MATLAB par que se torne uma toolbox do mesmo, chamada STAVBreach, especializado na simulação de rotura de barragens de aterro por galgamento.

O modelo foi validado para vários problemas bem conhecidos com soluções analíticas, que representam soluções particulares das equações de Saint-Venant em ambientes 1D e 2D, com e sem transporte de sedimentos.

O trabalho experimental levado a cabo no LNEC, forneceu os dados para modelar a rotura de barragens em modelos de pequena escala. Os resultados permitiram a obtenção de hidrogramas de cheia em várias localizações assim como a documentação do processo de rotura.

Finalmente foram levadas a cabo simulações numéricas de barragens semelhantes às testadas em ambiente laboratorial e os resultados foram comparados e discutidos.

Este trabalho mostrou a necessidade de considerar os deslocamentos de massas de solo durante o processo de rotura de barragens, e que o mecanismo de deslizamento escolhido consegue simular estes fenómenos.

Palavras-chave: Rotura de barragem, Modelação numérica, Equações de conservação, galgamento

Abstract

Water reservoirs are fundamental to socio-economic development of any civilization because they mainly provide water and energy. Increased demographic pressure has motivated the construction of dams to store water, therefore inducing flood hazards on downstream valleys. Dam failures lead to extreme economical losses, environmental damages and are likely to cause human casualties. They may fail due to various causes, being overtopping and piping the most common in earth dams (ICOLD (2013)).

An existing numerical model STAV2D was adapted to a new language with the purpose of producing a toolbox for MATLAB called STAVBreach, specialized in the simulation of breaching of embankment dams. Both the language and software used provide a more practical user interface for future work and learning.

The model was validated for several well known problems with analytical solutions that represent particular cases of the shallow water equations in both 1D and 2D environments with and without sediment transport.

Experimental work performed at LNEC provided the data necessary to model the dam breaching process in small scale dams with good geotechnical design requirements. The results obtained provided estimations of the breach hydrographs in different locations as well as a documented breaching process.

Finally numerical simulations were made for similar conditions as the experiments and the results are compared in order to validate the numerical model.

This work has demonstrated the need to consider mass displacement in the breaching process of dams in dam breach simulations, and that the geotechnical instabilization engine developed is able to simulate the mass displacement phenomena.

Keywords: Dam breach, Numerical modeling, Shallow water equations, Overtopping

Contents

List of Tables

List of Figures

Notation

A	Cell area	$[L^2]$
C	Sediment concentration	$[-]$
C_L	Homogenous, depth-averaged sediment concentration in layer L	$[-]$
C_f	Friction coefficient	$[-]$
c	Shallow water wave velocity	$[ms^{-1}]$
$\tilde{c}_{ik}$	Approximate c in k edge	$[ms^{-1}]$
d_s	Reference sediment diameter	$[m]$
$\tilde{e}_{ik}^{(n)}$	n eigenvector	$[ms^{-1}]$
$\mathbf{E}$	Flux vector	
$f_{s_{ij}}$	Stress tensor	$[Pa]$
$\vec{F}$	Generic force	$[N]$
$\mathbf{F}$	Flux vector in x	
$\mathbf{G}$	Flux vector in y	
g	Gravitic acceleration	$[ms^{-2}]$
$\mathbf{H}$	Source terms vector	
h	Fluid height	$[m]$
H	Average depth	$[m]$
h_L	Thickness of layer L	$[m]$
h_L	Fluid height on the left side of a shock	$[m]$
h_R	Fluid height on the right side of a shock	$[m]$
$\vec{n}$	Unit normal to a plane	$[m]$
K_s	Manning-Strickler coefficient	$[m^{1/3}s^{-1}]$
L	Wavelength (KdV notation)	$[-]$
L_l	Lower interface of a given layer	$[-]$
L_u	Upper interface of a given layer	$[-]$
p	Bed porosity	$[-]$
p	Hydrostatic Pressure	$[Pa]$
P_L	Depth-averaged hydrostatic pressure in Layer L	$[Pa]$
q_s	Solid discharge	$[m^3s^{-1}]$
q_s^*	Solid discharge capacity	$[m^3s^{-1}]$
$\mathbf{R}$	Friction source term vector	
s	Specific sediment gravity	$[-]$
S	Shock speed	$[ms^{-1}]$
$\mathbf{T}$	Bottom slope source terms numerical flux matrix	
T_{ij}	Depth integrated turbulent tensions tensor	$[Pa]$
u_ϕ	Velocity associated with the vertical mass flux	$[ms^{-1}]$
u_I	Interface velocity	$[ms^{-1}]$

u_L	Velocity on the left side of a shock	$[m]$
u_R	Velocity on the right side of a shock	$[m]$
u_*	Friction velocity	$[ms^{-1}]$
U_{i_L}	Depth averaged velocity in layer L, in the x_i direction	$[ms^{-1}]$
U_L	Depth averaged velocity in layer L, in the x direction	$[ms^{-1}]$
$\mathbf{U}$	Independent variables vector	
$\mathbf{V}$	Primitive variables vector	
V_L	Depth averaged velocity in layer L, in the y direction	$[ms^{-1}]$
w_i	Weight factor for cell i	$[m]$
w_s	Sediment settling velocity	$[ms^{-1}]$
Z_b	Bed elevation	$[m]$
$\alpha_{ik}^{(n)}$	Wave strengths in k edge	$[m]$
$\beta_{ik}^{(n)}$	Bottom source flux coefficient in k edge	$[m]$
δ_{ij}	Kronecker delta	$[-]$
ϵ	Depth-averaged turbulent kinetic energy rate of dissipation	$[m^2s^{-3}]$
ϕ	Generic function	$[m^3s^{-1}]$
θ	Shields parameter	$[-]$
κ	Depth-averaged turbulent kinetic energy	$[m^2s^{-2}]$
$\tilde{\lambda}_{ik}^{(n)}$	n eigenvalue of	$[ms^{-1}]$
λ_t	Wavelength	$[m]$
λ_L	Characteristics speed on the left side of a shock	$[m]$
λ_R	Characteristics speed on the right side of a shock	$[m]$
Λ	Adaptation length	$[m]$
μ	Dynamic viscosity of the fluid	$[Pa.s]$
ν	Poisson coefficient	$[-]$
ν_T	Turbulent viscosity	$[Pa.s]$
ρ	Mixture density	$[kgm^{-3}]$
ρ_L	Depth-averaged density of the mixture on layer L	$[kgm^{-3}]$
$\rho^{(w)}$	Clean water density	$[kgm^{-3}]$
$sigma_{ij}$	Stress tensor	$[Pa]$
τ_{ij}	Turbulent stress tensor	$[Pa]$
τ_b	Bed shear stress	$[Pa]$
τ_y	Yield stress	$[Pa]$
τ_v	Viscous stress	$[Pa]$
τ_t	Turbulent stress	$[Pa]$

Acronyms

BC	Boundary Conditions
CFD	Computational Fluid Dynamics
CFL	Courant-Friedrichs-Lewy
FEM	Finite Element Method
FDM	Finite Difference Method
FVM	Finite Volume Method
IC	Initial Conditions
RH	Rankine-Hugoniot (conditons)
RP	Riemann Problem
STAV-2D	Strong Transients in Alluvial Valleys 2D

Chapter 1

Introduction

1.1 Motivation

Water reservoirs are fundamental to socio-economic development since the beginning of human history. They mainly provide water and energy but many other secondary uses can be described from providing food (aqua-culture) to touristic activities. Although reservoirs can be natural, increased demographic pressure has forced making to build dams to store water, therefore inducing flood hazards on downstream valleys. Dam failures lead to extreme economical losses, environmental damages and are likely to cause human casualties. They may fail due to various causes, being overtopping the most common in earth dams (ICOLD (2013)).

The most recent advances in modeling the breaching process of embankment dams still encounter difficulties to correctly characterize the geotechnical processes associated to the episodes of sudden enlargement of the breach. The most common way of modeling these phenomena is by introducing a critical angle that, when the local breach slope becomes larger, causes a sudden enlargement of the breach sides leaving a residual or bearing angle.

There is a pressing need to better describe the mass instabilization episodes during dam overtopping and to effectively implement these phenomena in a numerical tool. The description of sediment transport in the dam body is, currently, also not entirely validated. These shortcomings in existing modeling approaches motivated the present work.

1.2 Objectives and Methodology

The main objective of this work is to develop a numerical model able to simulate the breaching process of embankment dams. It is designed to constitute the core of a toolbox for MATLAB, taking advantage of the capabilities of that graphical and computing software for user interface and graphical interface. The secondary major objective of the thesis is help develop the ongoing experimental work at LNEC, and participate in every phase of the process, in order to gather the necessary data for the validation of the numerical model.

The simulation tool, named STAVBreach (Strong Transients over Alluvial Valleys - Breach), is based on the shallow-water assumption, is meant to feature enhanced sediment transport capabilities and features simple but effective discretization scheme, based on a prior version. The discretization scheme belongs to the family of Finite Volume Methods, namely flux-vector splitting methods.

Developing a numerical simulation tool entails choosing a conceptual model, a discretization scheme and validation tests. The later stage was undertaken with theoretical solutions of the shallow-water and original laboratory work.

In what concerns laboratory work, dam-breach data from experiments conducted at LNEC was employed in order to assess model performance in real-world scenarios, by providing reliable and accurate measurements of the outflow hydrographs and a detailed characterization of the process. The experiments aimed at describing the breaching phenomena and obtain estimates of the outflow hydrograph or breaching hydrograph.

1.3 Thesis structure

The present work is divided into 6 chapters, the first of which is the introduction.

The second chapter is aimed at providing some notions of embankment dam design and properties as well as describing the failure of dams by overtopping and the main mechanisms involved.

In the third chapter, the experimental facilities at LNEC are described and the characterization and results of the two experiments conducted are presented.

The fourth chapter serves to present the conceptual model and the discretization scheme.

In chapter five the model is evaluated for several well documented problems which represent particular analytical solutions of the shallow water equations. The model is then used to simulate the breaching of an embankment similar to the ones produced for experimental work and the results are presented.

Chapter six is to present the conclusions for the study as well as some recommendations for future work.

Chapter 2

State of the art

2.1 Introduction

The basic needs of fresh water storage for human consumption, agriculture, flooding control, and waste management were the main reasons for the appearance of the first dams. According to Silva (2001) the earliest dams for which remains have been found were built around 3000 BC as part of an elaborate water supply system for the town of Jawa in modern day Jordan. Figure 2.1 represents Almonacid de la Cuba dam, an ancient roman gravity masonry dam dating to 1^{st} century AD.

Artificial dams can be made of concrete or soils, or of soil-rockfill. Earth dams are a viable choice, since they provide a very cost effective and stable solution if designed properly. The greatest problems faced when designing embankment dams, reside in the interaction between water and soil, meaning the dam should act as barrier to the passage of water, and problems that derivate from the water percolation should be minimized to avoid failure by piping.

Figure 2.1: Almonacid de la Cuba dam (Parra and Barranco, 2003).

Embankment dams are generically classified as follows (RSB, 2007):

- earth dams with homogeneous or a zoned profile;
- rock-fill dams with impervious protection on the upstream slope, or with an internal impervious protection such as a clay core;

- mixed dams with the longitudinal profile divided in two embankments, one earth and another rock-fill embankment or soil-rockfill mixtures;

There are also different types of embankment dams not covered by this classification because the design of the dam is inherently conditioned by the materials available on site.

The previous classification is based on the distinction of the different types of materials used to build earth and rock-fill embankments. The distinctive characteristics of the materials used are as follows:

- Materials used in the earth embankments, are mainly different types of soil that must guarantee both impervious and strength characteristics. Other types of materials such as concrete, soil-cement mix, steel, asphalt cement are used to create impervious walls inside the earth dam if the geomaterials available are not able to ensure the impervious characteristics.

- The different types of materials have an extensive grain size distribution.If soils, in general their predominant particle diameters smaller than 2 mm. The behavior of the embankment regarding the compaction, deformation structural resistance and permeability is conditioned by the fine matrix provided by the fine elements in the soil;

- Rock-fill material is defined by a high significant diameter ($D_{50} < 2\,\mathrm{m}$) and $\%(D = 50\,\mathrm{mm}) > 60\%$ and low presence of fine particles ($< 5\%$), with $K_{sat} > 10^{-5}$[1] (NEVES, 2002).

2.1.1 Types of embankment dams

Homogeneous Embankment Dams

Homogeneous embankment dams are generally composed by clay, sandy clay, clayey sand and clay mixes.

Because the embankment is generally composed of one type of material, it should be able to give the characteristics needed for a proper dam. The material must have low permeability, resistance and high stiffness(or enough stiffness).

The whole embankment acts as a control system for water seepage. Seepage control devices such as filter and drains are mandatory, and must be designed to avoid problems mainly associated to internal erosion and piping phenomena.

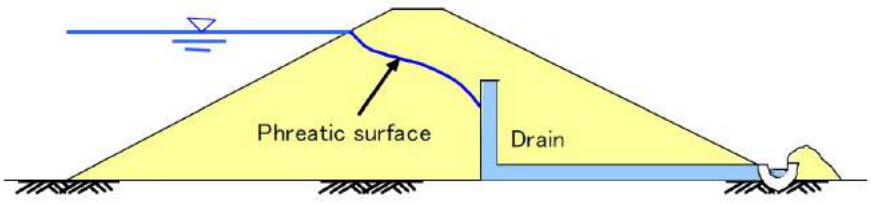

Figure 2.2: General profile for homogeneous embankment dam. (Source: Narita, 2000).

The main aspect to account for in designing homogeneous embankment dams is the seepage control. The saturation curve must be kept far from the surface of the downstream face of the dam in order to

[1] Hydraulic conductivity of saturated soil

avoid seepage in this slope and therefore failure by sliding in the downstream face. This can be ensured by introducing a filter and a drain. The addition of a drain on the downstream toe of the dam is used to avoid the problem, capable of capturing and draining the flow due to seepage trough the embankment's body and also trough the foundation. In figure 2.2 an example of the implementation of seepage control devices such as filters is presented.

Zoned embankment dams

Zoned embankment dams are a natural follow up from homogeneous embankment dams, and are very common because usually there is lack of fine materials near the dam site and the transportation costs of the soil increase, rendering the project costly. Also different zones in the dam allows for steeper inclines, making the dam use less material and therefore reducing cost. By zoning the dam profile, materials can be selected according to the design criteria for that zone, for example, clay can be used in the nucleus to make it impervious and a rock-fill layer can be used in the downstream slope and also in the upstream slope to guarantee the mechanical resistance of the dam.

The general profile for a zoned embankment dam is composed by soil, rock-fill and a clay core. In figure 2.3 an example of the profile for a layered embankment dam is provided.

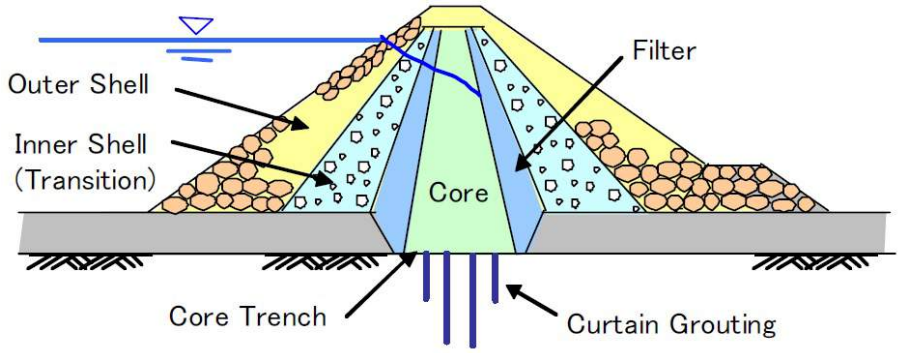

Figure 2.3: General profile for a zoned embankement dam. (Source: Narita, 2000).

In addition to the soil zones, there also the seepage control devices such as filters and drain to prevent internal erosion from the core.

Other types of zones dams have a synthetic impervious protection on the upstream slope or in the center. Materials used can be concrete such as in rock-fill dams with a concrete wall, or asphalt cement or even steel plates.

Rock-fill dams

Rock-fill embankment dams are a type of dam that have steeper slopes because of the naturally high friction angle of the material. Water seepage is naturally a disadvantage of this types of embankments due to the high permeability of rockfill material so seepage control mechanisms should be considered, such as the introduction of a structural concrete wall on the upstream slope, which is generally constructed over a layer of carefully selected rock-fill, to allow for uniform support conditions of the concrete

layer, as well as avoiding sliding. The concrete layer is placed against this selected rockfill layer, with sealed contraction joints, in order to prevent the concrete layer from cracking due to deformations produced by concrete retraction, embankment settlement, temperature variations and hydrostatic pressure.

Figure 2.4: Pego do altar Rock-fill dam with a steel layer on the upstream slope. (Source: O Leme - Imagens de Alcácer do Sal).

Other solutions include the ones presented with the layered embankment dams, such as an asphalt cement layer, or a steel protection as presented in figure 2.4 in the Pego do Altar dam, where a steel plate was used to cover the upstream slope.

2.1.2 Embankment dams. Geotechnical properties

Earthen embankments are mainly composed of clayey soil. Properties of the soil to account for in embankments design are:

· type of soil;

· grain size distribution;

· consistency limits;

· soil classification;

· compaction curve (dry density and water content);

· internal friction angle;

Grain size

For embankment dams, the grain size distribution of the soil allows for quality control of the dam. The construction process produces the refined grading size distributions in case of rockfill materials. In case of fine materials, the respective grading size distribution must be controlled during placement, as well as compaction characteristics. Each layer of the embankment must have homogeneous mechanical properties throughout. The quality control using the grain size distribution of the soil is also used to monitor the compaction process of the dam during, and after construction.

The size of the soil particles can be characterized by sieving tests, where the different grain size fractions of soil are separated according to a certain specification, for example the E-219 specification,

and are used to obtain grain size distribution curves where one can identify the representative particle diameter of a given amount of material that is captured by the screens.

Table 2.1 shows materials used in different zones of the embankment, the respective uses and properties.

Compaction

Compaction is a process to increase the resistance of the soil under constant water content conditions. The stress applied to the soil leads the pore air to be displaced and the particles to rearrange. Therefore this process increases resistance and decreases the permeability of the soil.

The process of compaction is different depending on the grains size of the soil. In fine soils, due to the size of the grain, electromagnetic forces are predominant (attraction and repulsion), and are highly dependent on water content. In granular soils, gravity is the predominant force that binds the particles together trough friction. There is insensitivity to the moisture content on the soil, making it necessary to rearrange the particles by vibrating the soil to acquire a denser soil by forcing the air out.

Water content of fine soils is vital to proper compaction. Water acts a lubricant within the soil, sliding the particles together (INC., 2011). For each type of soil, for a given energy it is possible to define a compaction curve as represented in figure 2.5.

There are two types of energy, given by the normal proctor method (D 698) and the modified proctor method (D 1557). In the compaction curve a wet side and a dry side can be identified as being to the left side of the optimum (lower water content) and to the right of the optimum (higher water content) for which the soil behaves differently as it was stated above.

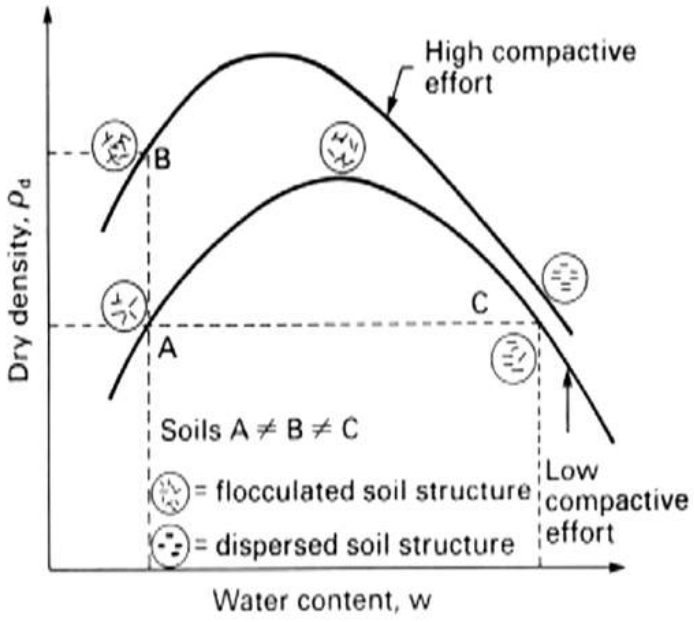

Figure 2.5: Compaction curve for different soils and compaction efforts. Comparison of different soil structures induced by compaction effort. (Source: Cardoso, 2010).

This is an important characteristic of the soil to be used in earthen embankments, since the dam

is susceptible to some degree of imposed deformations and movements over time, and if the soil is to rigid, cracks may appear and increase the rate of water flow trough the dam.This effect is particularly degrading in zoned dams, since the core is commonly composed of clay soil, that has a high volumetric expansion when in contact with water after drying.

Figure 2.7 represents silty clay compacted on the wet side leaving a smoother structure on the soil, and much smaller pores and figure 2.6 represents a sample of the same soil but compacted on the dry side, giving the soil a more flocculated structure (Alonso, 2004)

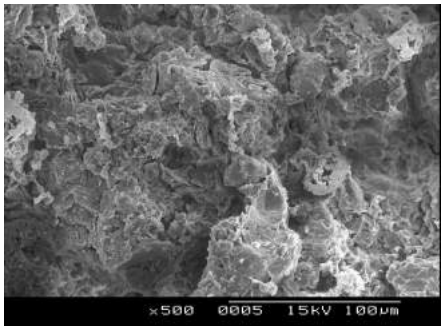

Figure 2.6: Silty clay compacted on the dry side. (Source: Alonso, 2004).

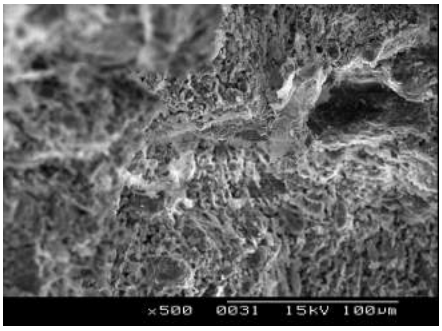

Figure 2.7: Silty clay compacted on the wet side. (Source: Alonso, 2004).

Embankment dams are usually compacted in the wet side of the reference curve in order to obtain less rigid soil with less volumetric expansion during the wetting process and the cycles of wetting and drying caused by the reservoir level variations during exploitation.

2.1.3 Elements of embankment design

Project Criteria

The fundamental project requirements for and embankment dam, regardless of the profile adopted are:

- Hydraulic resistance. Safety criteria and protective measures against seepage and internal erosion. Special attention must be given to scenarios of rapid filling and rapid draining of the dam as well as the behavior during the first filling.
- Structural resistance, the embankment body should be able to support the water pressure and the slopes must be stable in every design scenario during construction and exploration of the dam.

The safety requirements for embankment dams design are not limited to the sliding accidents of the embankment slopes, and the most important aspects to consider have to do with water seepage. The design criteria is verified whenever:

$$\tan \alpha_d < \tan \phi'_d \tag{2.1}$$

where ϕ'_d is the design effective internal friction angle of the material, α_d is the design embankment slope.

Upstream slope

The design for the upstream slope of the embankment dam is done for test scenarios during dam construction and during rapid drawdown conditions (Marcelino, 2008). The failure of the upstream slope is highly improbable for retention water level conditions since the oercolantion force acts as a stabilizing force on the upstream side of the embankment.

During construction if the soil used in the upstream embankment body has a high amount of fine material and the water content is close to or above the optimum, pore pressure is generated by the compaction efforts and by increasing gravity forces. This is the only situation when safety must be checked during construction. In service, for rapid drawdown conditions, if the material in the shoulders has low permeability (figure 2.8), pore pressure located in the upstream body do not have time to dissipate, in this case there is the inversion of the water flow trough the dam, causing the percolation force to be instabilizing.

Numerical simulations were conducted (Alonso and Pinyol, 2008) on the San Salvador dam for rapid drawdown conditions, in figures 2.8 and 2.9 the influence of the permeability for the pore water pressure, when in rapid drawdown conditions. In the first case problems may occur.

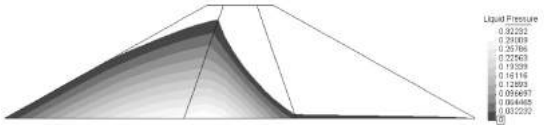

Figure 2.8: Pore pressure distribution after total drawdown in San Salvador dam, low permeability.

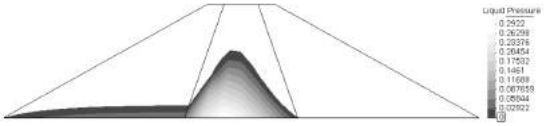

Figure 2.9: Pore pressure distribution after total drawdown in San Salvador dam, high permeability.

Downstream slope

The design of the downstream slope for the embankment body follows the same guidelines as the upstream slope, but for different conditions, during construction and for retention water level conditions. The first case should only be a factor when pore pressure is generated during construction. In service, the critical scenario should be wh the retention level (Marcelino, 2008). For these conditions the water load acts as stability-unbalance effect.

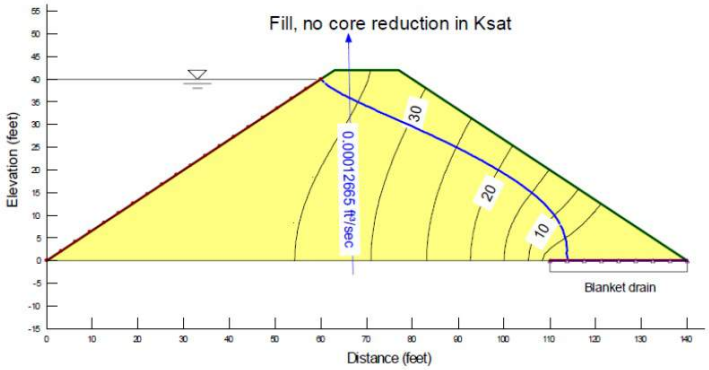

Figure 2.10: Flow line for embankment dam with retention water.(Source: (Cardoso, 2010))

The result is a higher α_d leading to a steeper slope compared to upstream, due to the fact that failure conditions are not influenced by rapid drawdown scenarios.

On the contrary, internal erosion phenomena needs a much more detailed design and analysis with a higher risk of failure. For example construction defects associated with the filters could lead to internal erosion of the core or to piping failure, or to the transport of material from the core to the voids on the rock-fill or embankment layers downstream. Internal erosion corresponds to the phenomena of transport of soil particles from the inside of the dam, by water seepage forces. Internal erosion tends to propagate upstream from an outlet point downstream, trough water passages in the dam, or pipes, until it reaches the upstream slope of the dam or the foundation surface also upstream. This type of failure is called piping and is one of the fastest to lead to the dam breaching.

Geological and geotechnical studies should be performed in order to gather information on the type and characteristics of the soil, localization of the ground-water level, local conditions, identification of geotechnical singularities such as seismic faults and others.

Element	Function	Materials used for construction
Soil	Seepage control trough the embankment	Clay, sandy clay, clayey sand, silty sand, some amounts of gravel is allowed. Generally more than 15% have dimensions lower than 75 μm.
Fine filter	Prevent water seepage trough the embankment. Avoid internal erosion of the foundation when used as a draining carpet. Avoid the increasing pore pressure on rhe downstream slope when used as vertical drain.	Sand of sand with gravel, with less than 5%(preferably 2%) of particles with diamiters lower than 75 μm. The fines materials used should not ble plastic. Layers should be constructed with materials obeying the same criteria for durablity and hardness as concrete agregates. The particle dimensions have to obey the filter condition.
Coarse filter	Avoid erosion of the materials from the fine filter. Drain seepage water colected on the vertical drain or the draining carpet.	Sand with gravel of sandy gravel. Layers should be constructed with materials obeying the same criteria for durablity and hardness as concrete agregates. The particle dimensions have to obey the filter condition.
Upstream filter/ Upstream rock-fill filter	Avoid erosion of the internal soil layer beneath the upstream rockfill and rockfill protection layer.	Sand with gravel or well graded sandy gravel, with 100% of the particles with a diameter lower than 75 mm and no more than 8% of those particles with a diameter lower than 75 μm. The fines used should not be plastic. The requirements for durability and hardness are less accurate than the other types of filters presented.
Rock-fill	Grant stability to the embankment body. Drain the water flow trough or under the dam. Avoid erosion of the filter, in the case where the filter is designed with a layer of coarse rockfill	Rockfill, preferably dense and resistant, and able to drain well after compaction, but more often materials with lower standards are also accepted. The rockfill is compacted in layers ranging from 0,5 to 1,0 m in thickness. The maximum particle diameter is equal to the layer thickness adopted.
Coarse rock-fill	Designed to give stability to the embankment body and drain water that passes trough or under the embankment.	Same materials and criteria used in Rockfill, but with layer thickness ranging from 1,0 to 1,5 m, and the same criteria for maximum particle diameter.
Rock-fill for protection layer	Avoid erosion of the upstream slope due to the wave action.	Carefully selected rockfill to fulfill the requirements of durability and stablity necessary to avoid erosion of the slopes under wave action.

Table 2.1: Overview of materials used in embankment dams and respective properties and functions. (Source: Caldeira, 2001).

2.2 Failure of Embankment Dams

2.2.1 Failure concept applied to embankment dams

Dam safety comprises the following criteria (RSB, 2007):

- Structural safety corresponding to the endurance and ability to satisfy the structural behavior demands related to performance in exploration situations as well as exceptional conditions and loads.
- Hydraulic safety regarding the behavior of the security devices and exploration components of the dam, as well as the filtering, waterproofing and draining systems.
- Operational safety corresponding to the capability of the dam to satisfy the behavior criteria related to operation and functionality of the equipments and safety and exploration components.
- Environmental safety corresponding to the ability of the dam to keep the demands for behavior relative limitation of incidents that might cause harm to the environment, namely to populated and productive areas.

Should any of these criteria not be met, the dam can be considered as in failure.

According to Singh (1996) the most common causes and modes of failure of earth dams are:

1 - overtopping caused by extreme floods;

2 - structural failure due to internal erosion (piping);

3 - structural failure due to shear slide;

4 - structural failure due to foundation defects;

5 - failure due to natural or induced seismicity;

This work will focus on structural failures related to intense precipitation events,earthquakes or any other actions that may cause a breach in the dam, leading to the flooding of the downstream areas.

2.2.2 Failure by Overtopping

The following section will focus on the first cause of earth dam failure, overtopping, giving the base mechanics of the process of failure and their main causes. A brief revision is made on the recent advances in dam breaching, most notably the implementation of algorithm to simulate the sudden collapse of parts of the breach wall, also known as sliding.

Three elements are included in the hydraulics of flow over the dam: flow over the crest, flow trough the breach and flow trough the breach channel on the downstream face of the dam. When the flow passes over the crest, the breach is formed.

The erosive force is highest on the downstream slope of the dam, because of the higher velocities the flow attains. The extent of erosion and subsequent sediment transport depend upon the extent of overtopping, material composition, downstream conditions (Singh, 1996).

Zhao et al. (2013) described the breaching process in 5 phases for sand embankments:

I - Steepening of inner slope from initial value;

II - Yielding a decrease of the width of the crest of the dike in the breach;

III - Lowering of the top of the dike in the breach, with constant angle of the critical breach side slopes, resulting in an increase of width of the breach;

IV - Critical flow stage, in which flow is virtually critical throughout the breach and the breach continues to grow mainly laterally;

V - Subcritical stage, in which the breach continue to grow, mainly laterally due to the subcritical flow in the breach;

In the first three stages the initial breach cuts itself into the dike and most discharge through the breach happens at stage IV and V.

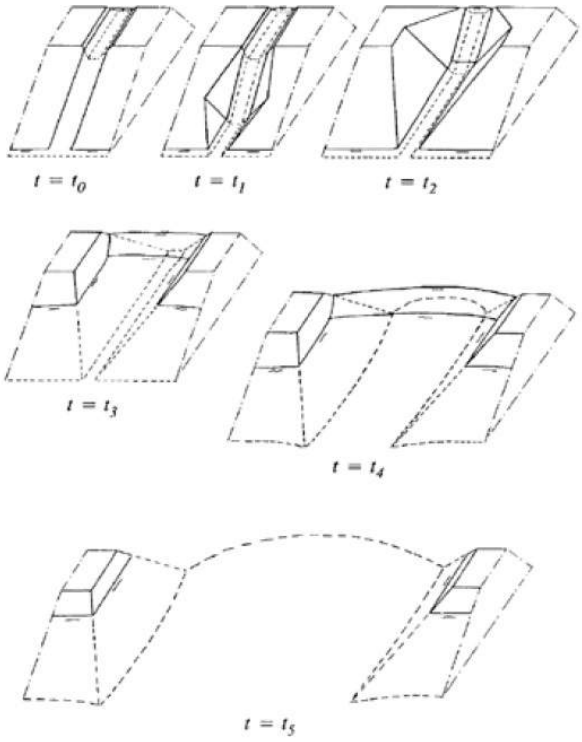

Figure 2.11: Stages of sand embankment breaching process described. (Source: Zhao et al., 2013).

2.3 Numerical modelling of dam breaching

In this section a brief description is given of the current state of numerical modelling of dam breaching processes.

The modeling of the breaching process in a non-cohesive soil embankment involves two different physical phenomena: surface erosion and bed displacement due to the shear velocity of the flow on the bed, and lateral erosion due to the instability of the breach sides (Emelen et al., 2015).

The first is a phenomena resulting from the interaction between the fluid layer (clear water layer and contact or transport layer) and the sediment bed. If the stresses on the boundary of the contact layer are not in equilibrium with the bed, there will be a bed variation as a consequence in the form of erosion. There is an equilibrium length or adaptation length, which is the distance needed for erosion and deposition phenomena to be in equilibrium i.e. for the bed variation over time to become null.

Surface erosion can be modelled by introducing a sediment conservation equation, coupled with the shallow water equations that relate the conservation of mass and momentum within a domain.

The second is is gravitational induce side wall failures (Volz et al., 2010).The failures occur spontaneously over the breaching duration and are usually the main cause for the lateral widening of the breach channel. Failure types can differ largely depending on various factors as e.g. the soil material, the seepage line and the pore pressures within the soil matrix. The majority of the observed failures types are a mix of fall and slide failure (Pickert et al., 2004).

Emelen et al. (2015) tested several sediment transport formulations, and some bearing angles for slope instabilization which where validated with laboratory experiments conducted in the Hydraulics Laboratory of the Université Catholique de Louvain, Belgium (Spinewine et al., 2004).

The numerical formulation used for the dam breaching simulations was:

$$\frac{\delta U}{\delta t} + \frac{\delta F(U)}{\delta x} + \frac{\delta G(U)}{\delta y} = S; \tag{2.2}$$

$$\boldsymbol{U} = \begin{bmatrix} h \\ uh \\ vh \\ z_b \end{bmatrix}; \quad \boldsymbol{F} = \begin{bmatrix} uh \\ u^2h + \frac{gh^2}{2} \\ uvh \\ \frac{q_{s,x}}{1-\epsilon_0} \end{bmatrix}; \quad \boldsymbol{G} = \begin{bmatrix} uh \\ uvh \\ v^2h + \frac{gh^2}{2} \\ \frac{q_{s,y}}{1-\epsilon_0} \end{bmatrix}; \quad \boldsymbol{S} = \begin{bmatrix} 0 \\ gh(S_o x - S_f x) \\ gh(S_o y - S_f y) \\ 0 \end{bmatrix}; \tag{2.3}$$

where x and y represent the components in x and y directions, respectively, and u and v are the depth averaged velocities in the x- and y-directions. q_s represented the sediment rate discharge and was estimated using a large number of well known empirical formulas.

The 2D bank-failure operator was developed and inserted into the classical 2D shallow model by Swartenbroekx et al. (2010). The operator is based on a local bank-failure criterion: the slope of each cell is calculated in order to analyse its stability. When the slope of a cell exceeds a critical angle α_c, the bank-failure is activated and cells are tilted until reaching a residual angle α_r

The numerical simulations obtained, presented in figure 2.12 show a good representation of the breaching process of sand dams. Tough is rarely the case, as explained in the previous chapter, design criteria for embankment construction are very demanding in terms of the materials used and construction techniques, thus, rendering the real life behavior of a dam when in a situation of overtopping very different, more notably the existence of undercutting when water is eroding the sides of the breach, which in turn leads to mass displacement phenomena and instantaneous breach enlargement. This phenomena does not occur in sand dikes.

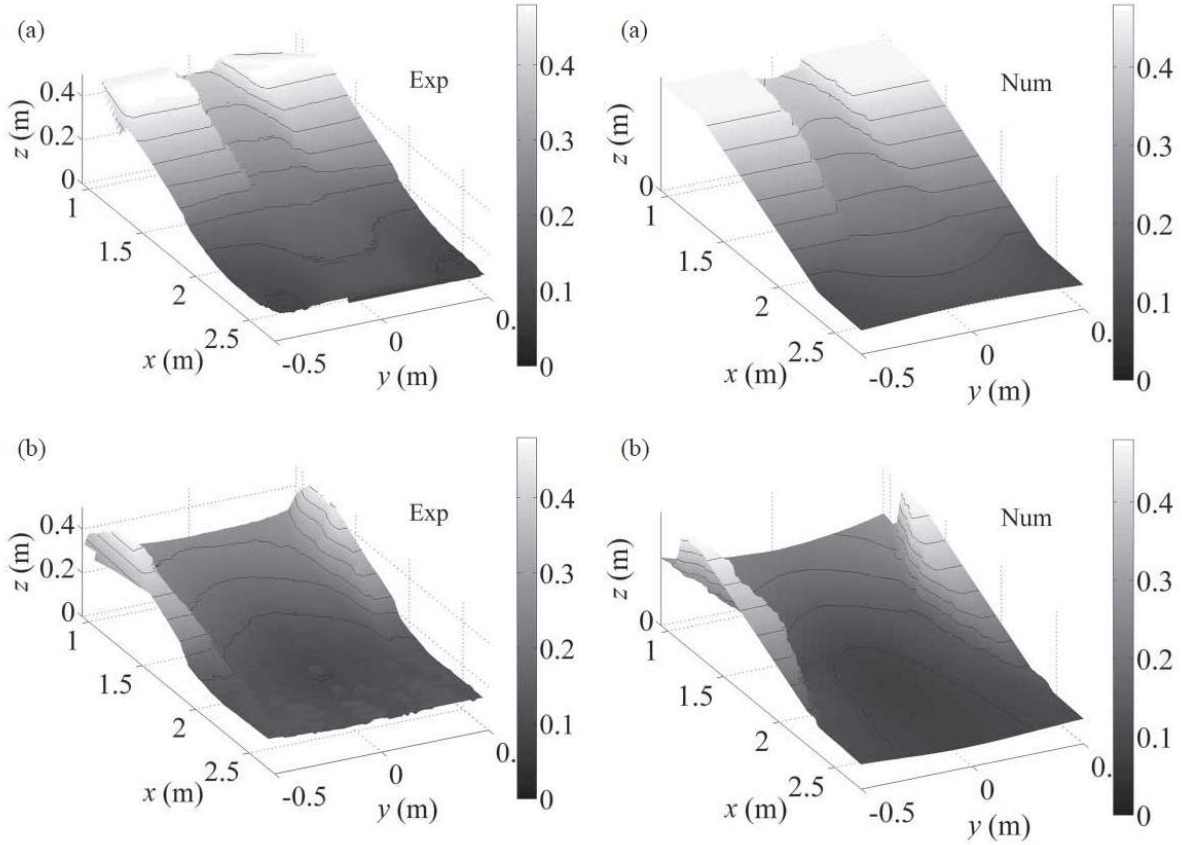

Figure 2.12: Dam breaching numerical simulation. (Source: Emelen et al., 2015)

.

Dual mesh approach

Using the same criteria for sliding failure, i.e. the critical slope angle, Volz et al. (2010) used a 2D dual mesh physically based model to simulate embankment dam breaching using surface erosion and geotechnical failure mechanisms. It used a separate mesh for the bottom, differentiating different significant grain diameter classes in order to better simulate the fluid-water interactions in the contact load layer. The discretization scheme is represented in figure 2.13.

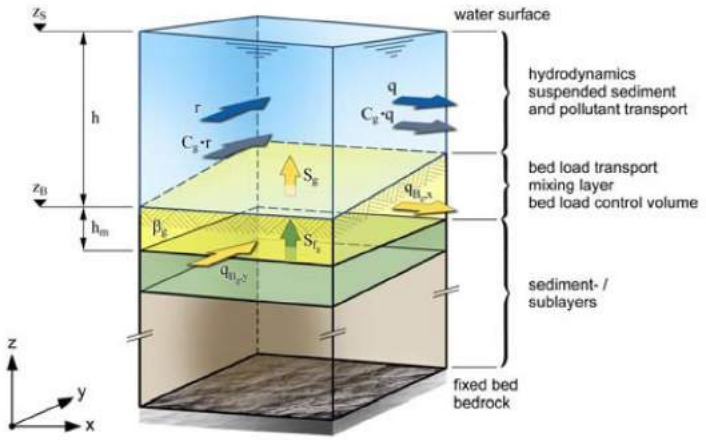

Figure 2.13: Discretization scheme for the dual mesh approach. (Source: Volz et al., 2010).

An Euler-scheme and Riemann-solver were applied to calculate the fluxes at the edges of the cells and for the solution of the balance equations an uncoupled, quasi-steady solution procedure was chosen.

The dual mesh approach leads to several numerical problems that can be summarized as (Volz et al., 2010) and represented in figure 2.14.

- Changes in the sediment volume of a cell by in- or out-flowing sediment fluxes must be distributed in an appropriate way on the nodes of this cell. However, the distribution of the sediment volume is not unique and it is not clear by which criteria it should be done
- Changes in bed elevation of a cell's node do not only affect the sediment volume of this cell, but also the sediment volumes of all adjacent cells. This is problematic regarding the conservation of the sediment masses
- These mutual influences between adjacent cells correspond to diffusive fluxes between the cells. In case of fractional transport this may lead to an undesired mixing of the grain compositions.

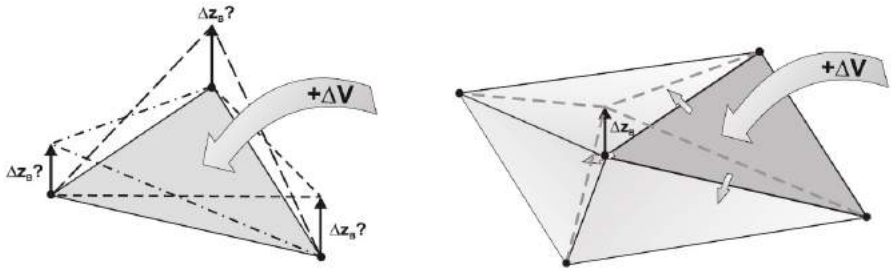

Figure 2.14: Dual mesh approach, numerical problems. (Source: Volz et al., 2010).

Numerical simulations of dam breaching where carried out, using and MPM (Meyer-Petter & Muller) formula to model surface erosion and a critical slope angle for sliding failure. The dam was divided in half, assuming symmetry in the response of the dam to the flow, to aid in computational efficiency.

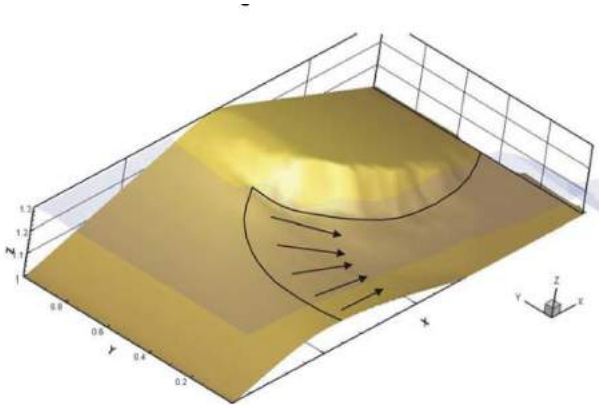

Figure 2.15: Simulated dam breach. (Source: Volz et al., 2010).

The results shown in figure 2.15 where compared with experimental data obtained by Pickert et al. (2011), where embankment dams where made similar fashion to the numerical model, i.e. only half of the dam was represented and symmetry along the longitudinal dimension of the dam was assumed, allowing

for a glass wall to be installed and monitor the breaching. The embankment was built up with three different uniform granular sands on a fixed bed.The comparison between numerical and experimental results is presented in figure 2.16.

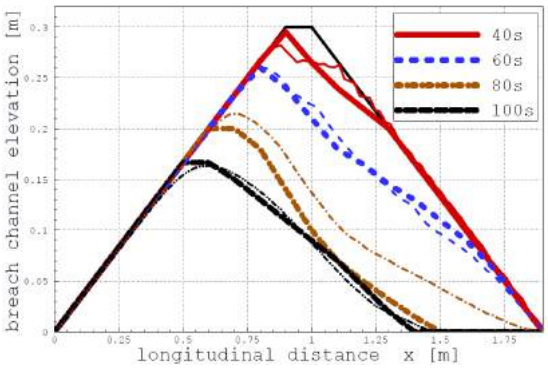

Figure 2.16: Dam breaching results and comparison with experimental data. (Source: Volz et al., 2010).

The results seem to show good agreement with the sand embankment breaching, and it is noted that one of the shortcomings of the lateral erosion modeling is that it occurs steadily and and continuously, which leads to small changes in the side wall slopes during the breaching, instead of massive events that lead to instantaneous breach enlargement (Volz et al., 2010).

The cases presented in this chapter study the breaching of sand embankments and are able to reproduce the breaching to some degree of accuracy, but earth dams are mainly composed of cohesive soil, and thus the breaching process is different due to the nature of the material, but also difficult to test due to the specifications needed to build properly compacted embankments and to the difficulty associated to characterize the complex breaching process of embankment dams.

Chapter 3

Dam breach experiments for model validation

3.1 Introduction

Experimental work was considered as a way of validating the numerical model. A reliable characterization of the breaching of embankment dams is crucial for a good calibration of the numerical model.

The experimental work was conducted at the National Laboratory of Civil Engineering (LNEC), in Lisbon, Portugal. Four experiments where undertaken in total. Between experiments, initial breach geometry and moisture content of the soil where changed to analyze the influence of each in the dam breaching process.

For this work it is reminded that the main objective of the experiments is to provide outflow hydrographs and a good documentation of the breaching experiments, that can be used to calibrate and/or validate the numerical model.

3.2 Overview of experimental setup

Figure 3.1 shows the floor plan and profile of the experimental setup, the following section will present the different equipments used in the experimental setups.

The model is not aimed at reproducing a real embankment dam. The goal is to induce dam breaching, while maintaining the cohesive nature of the dam material and compaction properties, which are observed in real life scenarios, but within a time frame suitable for the experiments, as due to the constraints of the experimental setup i.e. reservoir capacity and available materials and work conditions. In laboratory environment, if the criteria used for the models construction, would be the same as those for real dams, breaching would take too long to occur to be feasible.

1 - Flow inlet(Ø350 mm)
2 - Brick wall to still the flow at the reservoir inlet
3 - Resitive Probe (R1)
4 - Resitive Probe (R2)
5 - Resitive Probe (R4)
6 - Resitive Probe (R3)
7 - Resitive Probe (R5)
8 - Dispensador de poliestireno
9 - Acoustic probes
10 - Embankment
11 - Stilling pool
11 - Downstream spillway

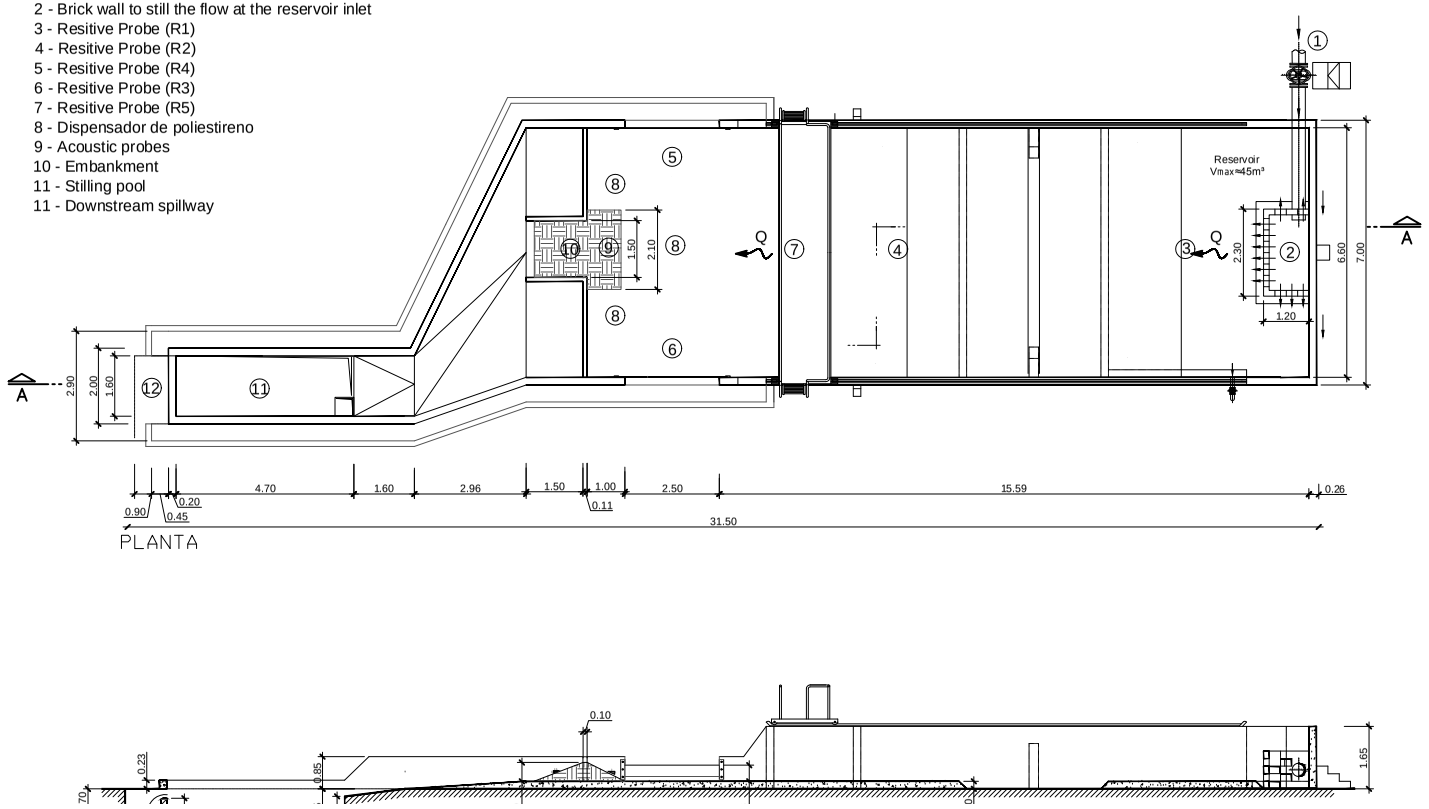

Figure 3.1: Experimental Facility for dam breach experiments

The set-up consists of a channel $31.5\ \mathrm{m}$ long, between $6.60 - 1.70\ \mathrm{m}$ wide and between $0.5 - 1.30\ \mathrm{m}$ deep. At the downstream end of the channel there are a sediment supply tank with $1.7\ \mathrm{m}$ width, $4.4\ \mathrm{m}$ length and a maximum depth of $0.60\ \mathrm{m}$, and a rectangular spillway.

The inlet, outlet and reservoir are instrumented with a flow meter and a total of six resistive probes respectively. A control volume sufficiently near the breach channel is instrumented with seven acoustic probes on the boundaries, two high speed motion capture cameras, one pointing downwards to the control volume, and the other pointing to the upstream face of the dam, in the direction of the breach channel. A laser equipped with prismatic lens is also implemented directly over the breach channel. A physical trigger in the form of a button was used to synchronize the data acquisition from the probes.

Upstream Inlet

The water storage in the underground reservoir is pumped to a reservoir located at higher altitude, and conducted to the channel by gravity. Due to the importance of maintaining a stable water surface level in the reservoir, a flow meter monitors the inflow. The structure seen in figure 3.1 2 is a brick wall designed to dissipate energy so that the laminar flow can be considered.

Spillway

The spillway (3.1, 11) will discharge the water volume from the embankment. It is equipped with a resistive probe to monitor the water height, and with an appropriate spillway equation, a an outlet discharge can be estimated.

3.3 Equipment and software

Acoustic Probes

The acoustic probes are able to determine the distance to an object or surface, by measuring the voltage needed to send a signal and measure the echo, the measurement can then be translated into distance with the appropriate calibration.

An example of an acoustic probe is presented in figure 3.2

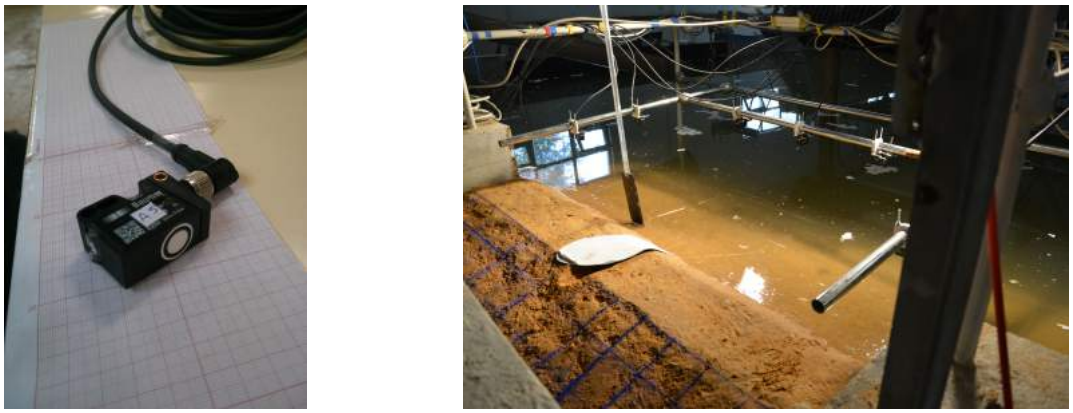

Figure 3.2: Acoustic probes overview and placement

Resistive Probes

The use of the resistive probes is based on the principle that the conductivity between the electrodes is directly proportional to their immersed length.

Figure 3.3: Resistive probe overview and placement

Figure 3.3 show an overview of the probes used, and an example of the placement inside the reservoirs. Five resistive probes were placed on the upstream reservoir to achieve a better description mass conservation of the water inside the basin during the breaching. The probes placed inside the reservoir coupled with the sixth one near the spillway and the flow meter on the inlet are able to provide an indirect estimation of the breach hydrograph.

Spider8

The hardware Spider8 was used to control and synchronize the data from the resistive probes and is presented in figure 3.4.

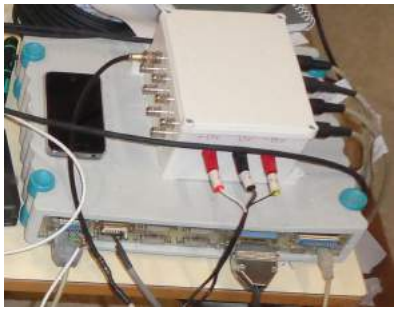

Figure 3.4: Spider8 signal amplifier

CatmanEasy

The data capturing software CatmanEasy was used to perform the data acquisition of the resistive probes and the flowmeter.

National Instruments data acquisition board

A data acquisition board made by National Instruments was used to acquire the data from the resistive probes and is presented in figure 3.5.

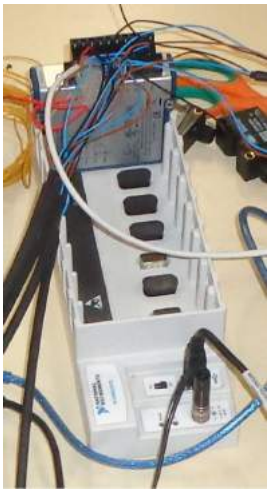

Figure 3.5: National instruments data acquisition board

LabView Signalexpress

The data acquisition software LabView Signalexpress was used to capture the data from the seven acoustic probes.

Trigger for data acquisition

Due to the nature of the equipments used and their compatibility with the various capture boards and different softwares, there is a need to carefully synchronize the data acquisition from all the probes involved, hence a physical trigger was developed to send a user generated tension peak that is registered at the same time in both data acquisition softwares and boards.

The external trigger is presented in figure 3.6.

Figure 3.6: Analogic Trigger for data synchronization

Photonfocus high speed camera

The Photonfocus high speed camera presented in figure 3.7 was used to document the dam breaching evolution. The camera was placed facing the upstream slope of the dam. Refraction effects of the camera lens where taken into account, as well as distance to the embankment breach and angle of the camera.

Figure 3.7: Photonfocus camera

Mikrotron high speed camera

The Mikrotron high speed camera was used to record images of the dam breaching process but more importantly, to monitor the passing of carefully selected styrofoam balls inside the control volume, so that a PIV algorithm can be applied and the velocity field near the breach channel can be estimated. This requires the acquisition framerate of the camera to be high and consistent enough that the position of the styrofoam balls can be tracked between two consecutive frames. The camera is presented in figure 3.8.

Figure 3.8: Mikrotron high speed camera setup

Ilumination setup

The high speed cameras need to be able to distinguish and isolate the styrofoam balls, and as such the experimental setup requires homogeneous lighting conditions inside the control volume, this was achieved by using a very low environment light, coupled with spotlights pointing to the control volume, as represented in figure 3.9.

Figure 3.9: Ilumination setup and purpose

Laser Quantum Finesse

The Laser was used to accentuate the dam breach geometry, when captured by the Photon Focus camera. A prismatic lens was placed directly under the laser and rotated so that the laser turns into a sheet of light, which when pointed towards the dam breach, should provide an accurate reading of the breach geometry. The laser is presented in figure 3.10.

3.4 Dam breaching experiments

3.4.1 Characterization of the embankments

Tests where performed to evaluate the geotechnical characteristics of the soil in order to choose a compaction method and effort adequate for the models. If the dam is built with realistic design param-

Figure 3.10: Laser used for dam breach monitoring

eters, then the breaching process should be able to be reproduced and the observed events should be similar to the events observed in similar real embankment dams.

Soil classification

Soil classification was obtained by performing screening tests and consistency limits tests.

Two soil samples are presented in figure 3.11. They were analyzed because they were stored in different places: indoor and outdoor.

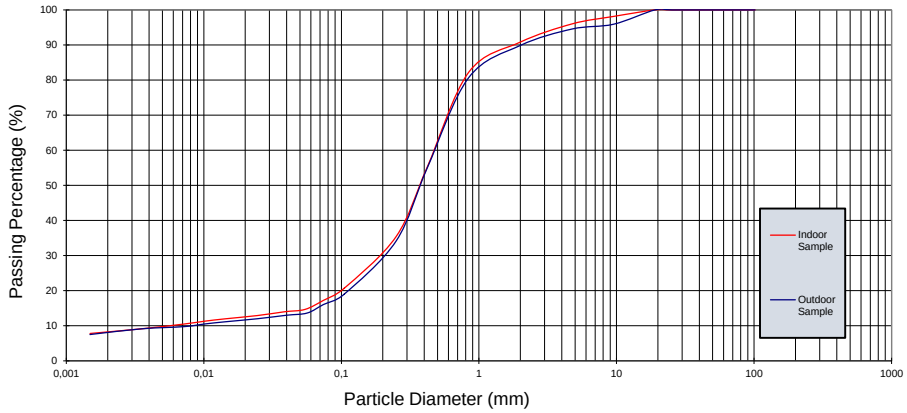

Figure 3.11: Grading size distribution curves

It was concluded that the storage methods had little impact on the grading size distribution curves because the two curves are very similar.

The results from the Atterberg limits tests revealed the soil to be non plastic (NP).

Using results obtained and according to Unified Soil Classification System, the soil was identified as silty sand (SM).

Compaction

Compaction tests where performed on the both soil samples acquired, and combined to create the compaction curve presented in figure 3.12. Standard compaction effort was applied following ASTM D-698.

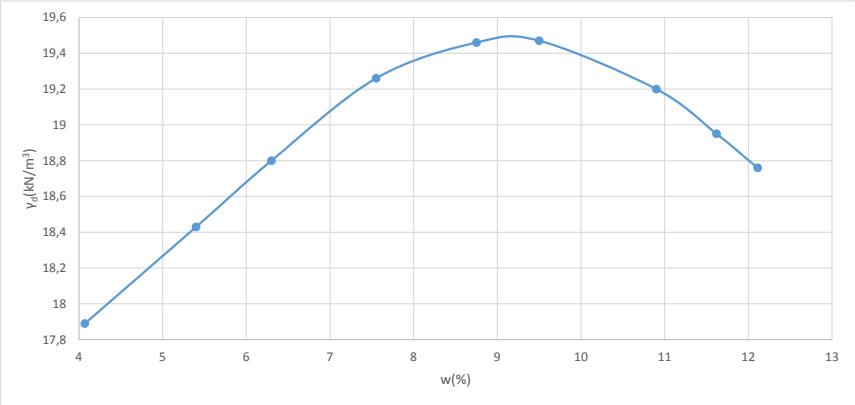

Figure 3.12: Combined compaction curve for both samples

The optimum point was identified and is presented in table 3.1.

Optimum point	
w(%)	γ_d (kN/m^3)
9,5	19,5

Table 3.1: Optimum point for compaction curve

This curve provides the optimum dry density and water content for compaction of a real embankment, however, model scale has to be accounted for, or else breaching will not occur. For this reason, a new compaction curve was obtained using 25% of the energy in the standard proctor test. The curve obtained is presented in figure 3.11.

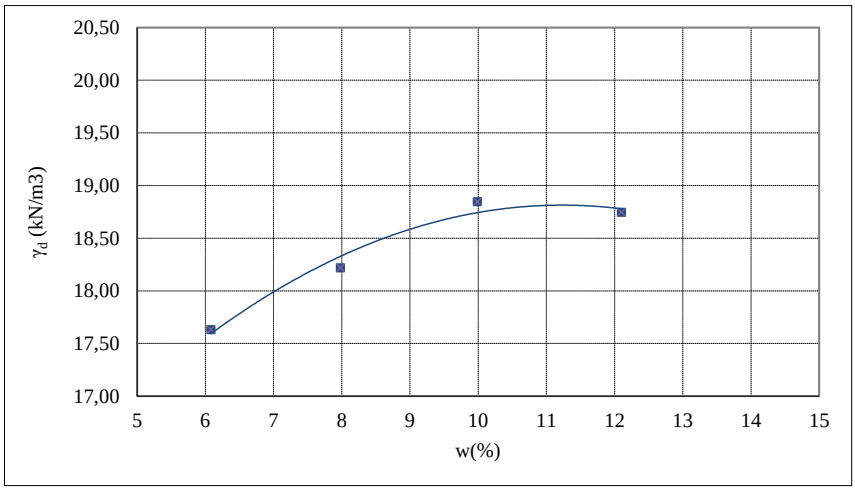

Figure 3.13: Compaction curve for 25% energy

The equipment used for compaction of the experimental embankments was the manual compactor PC1010 of Euroshatal weighting 46 kg, with a compaction area of 430 m^2/h and a vibration frequency of 100 Hz and is presented in figure 3.14.

More information about the experimental setup and embankment construction can be found in B.2 and in Santos (2015).

Figure 3.14: Manual compactor used in the experimental setup

Embankment geometry

Two embankments were built using the appropriate compaction techniques detailed in Santos (2015). The initial and post compaction profiles of the embankment are shown in figures 3.15 and 3.16.

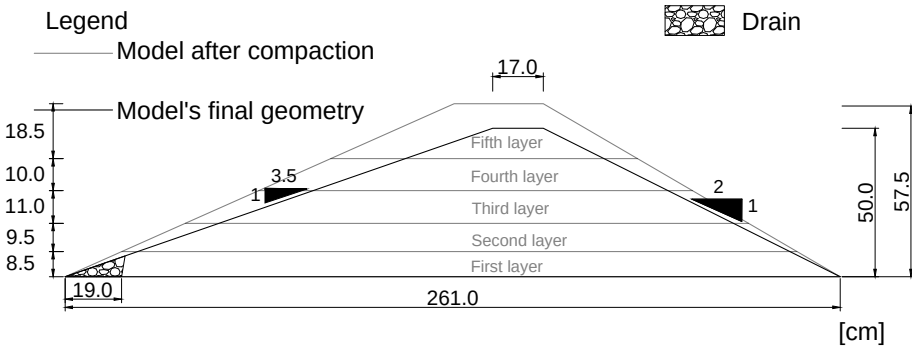

Figure 3.15: Comparison of profiles for the first embankment before and after compaction. Embankment 1

The main difference between embankments was the geometry of the pilot channel. In embankment 1 a triangular pilot channel,figure 3.17, was used with the dimensions $height = 5\ \mathrm{cm};\ width = 10\ \mathrm{cm}$ and in embankment 2, a rectangular pilot channel, figure 3.18, with $height = 5\ \mathrm{cm};\ width = 10\ \mathrm{cm}$.

The initial breach shape for experiment 1 was triangular, as it was expected to force the erosion progress downwards before the breach side could enlarge significantly. The geometry of the breach is presented in figure 3.18.

The different breach geometries were chosen to test the influence of the pilot channel shape in the overall evolution of the breach. For experiment 1 it is expected to force the erosion progress downwards before the breach side could enlarge significantly. For experiment 2 since the breach shape is more uniform it was expected that this type of channel would influence a more uniform erosion process on the breach bottom and walls.

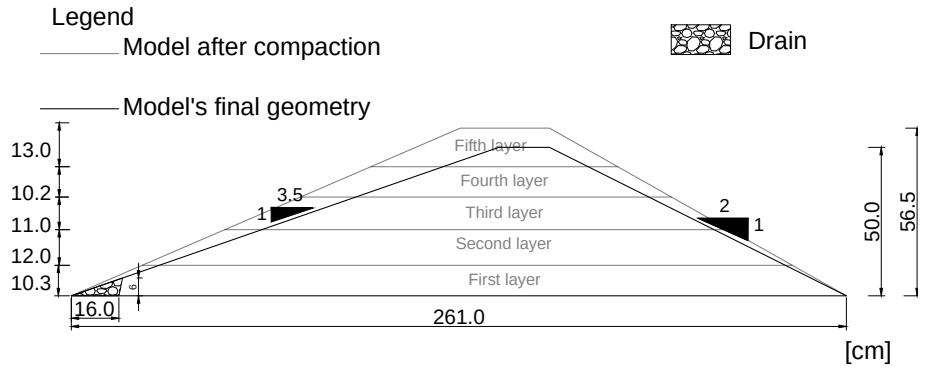

Figure 3.16: Comparison of profiles for the second embankment before and after compaction. Embankment 2

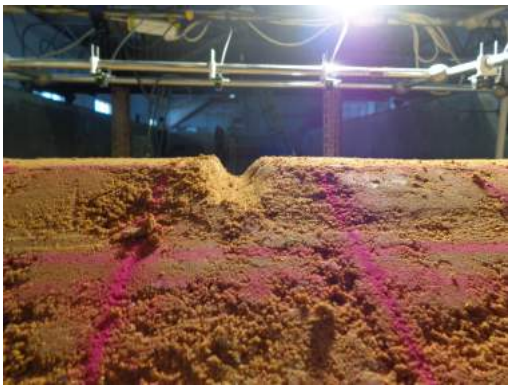

Figure 3.17: Initial breach geometry for experiment 1

Figure 3.18: Initial breach geometry for experiment 2

It is worth to mention that a drain was also built bellow the downstream slope in order to simulate an homogeneous dam. This drain might have influence in the overall evolution of the breach as discussed by Santos (2015). The drain is presented in figure 3.19

Figure 3.19: Drain placed at the toe of the embankment model.

Data collected and outflow hydrograph

As explained in the beginning of the chapter the probes placed on the experimental setup where used to gather water surface elevation, inside the reservoir, inside the area of influence near the breach and in the downstream spillway. Image and video recordings where taken from the high speed cameras and HD recording cameras placed in the setup.

The surface elevation measurements taken for the probes are presented in Figures 3.20 and 3.21 along with the discharge measured from the Resistive probe R6 placed on the spillway.

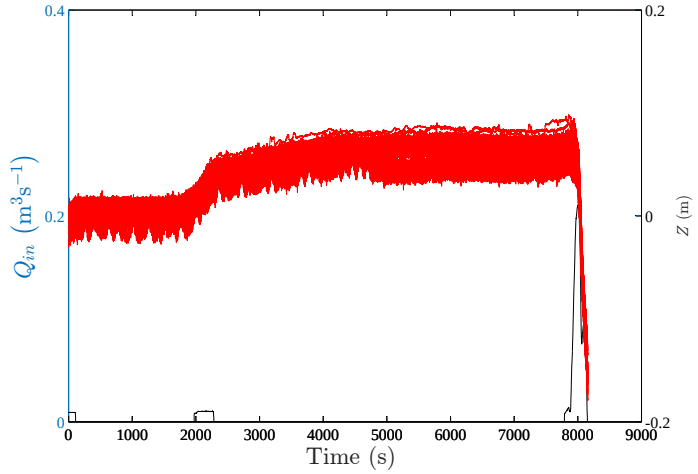

Figure 3.20: Surface elevation measurements for all probes vs discharged measured. Trial 1

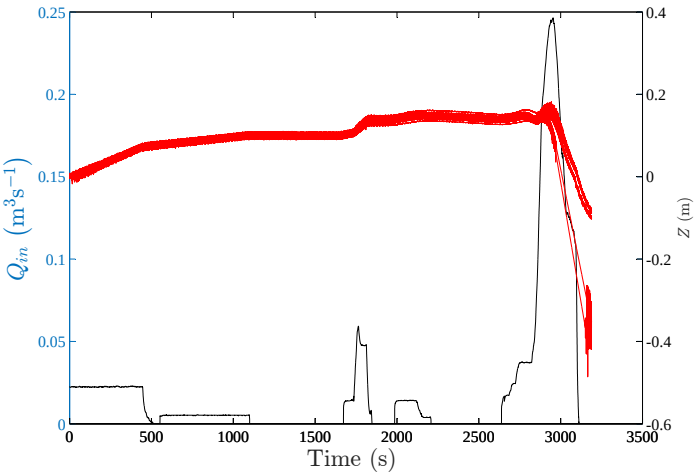

Figure 3.21: Surface elevation measurements for all probes vs discharged measured. Trial 2

The Discharge is measured at the inlet. In the outlet a spillway equation is applied using the elevation measurements taken from the probe. The discharge is then calculated by:

$$Q_{spill} = 140.74H^3 - 5.38H^2 + 0.4H \tag{3.1}$$

In the reservoir the discharge upstream of the breach channel is calculated using the conservation of mass equation inside the reservoir area. An influence area is attributed to each probe, by voronoi polygons as presented in figure 3.22

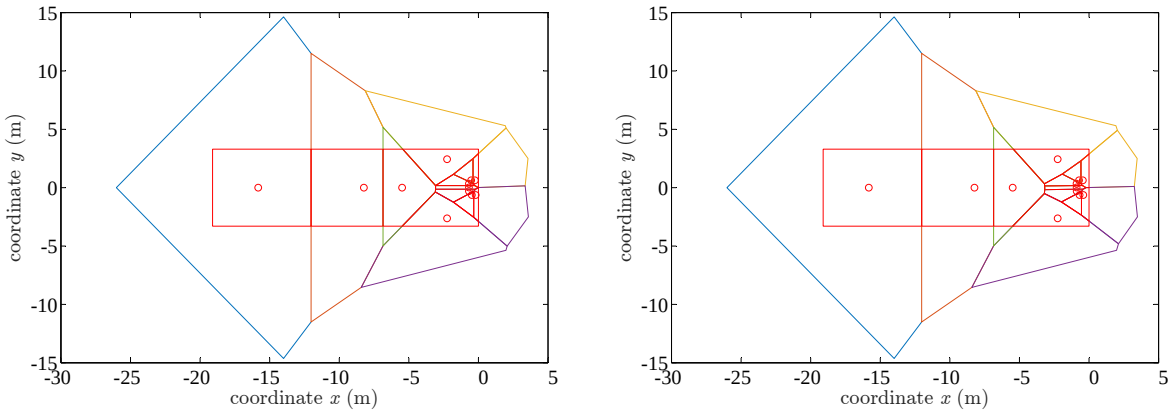

a) Trial 1 b) Trial 2

Figure 3.22: Influence areas for probes using Voronoi polygons

The flow upstream of the breach is then given by:

$$Q_{out} = Q_{in} - Area \times \frac{\delta Z}{\delta t} \tag{3.2}$$

where Q_{in} is the discharge measured by the flow-meter, Q_{out} is the discharge trough the breach, calculated upstream.

The data from the probes is then filtered and averaged to obtain the outflow hydrographs, presented in figures 3.23 and 3.24.

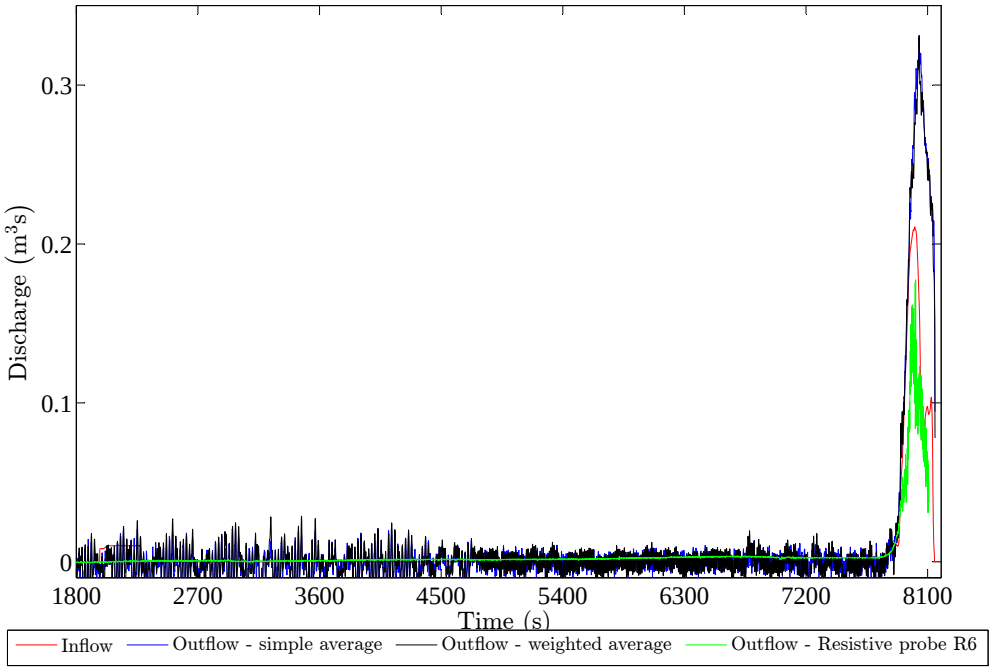

Figure 3.23: Outflow hydrographs for trial 1

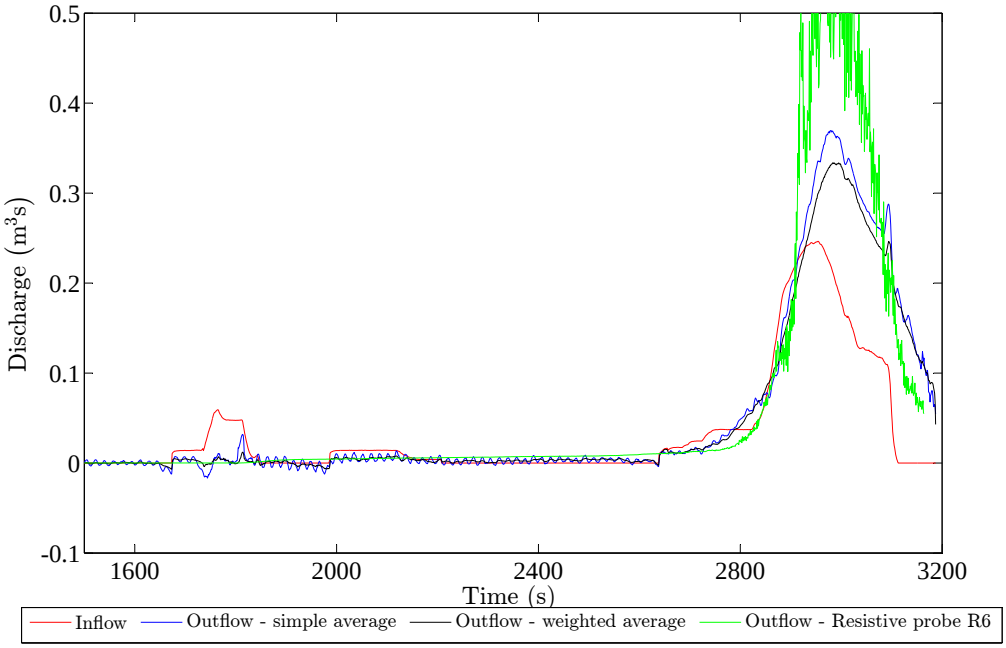

Figure 3.24: Outflow hydrographs for trial 2

Chapter 4

Numerical Model

4.1 Introduction

This chapter is aimed at the presentation of the numerical model used for the dam break simulations. The model was developed based on the conceptual model proposed by Ferreira (2005) which features conservation equations derived within the continuum approach for an idealized layered domain composed by the bed, transport layer and clear water layer.

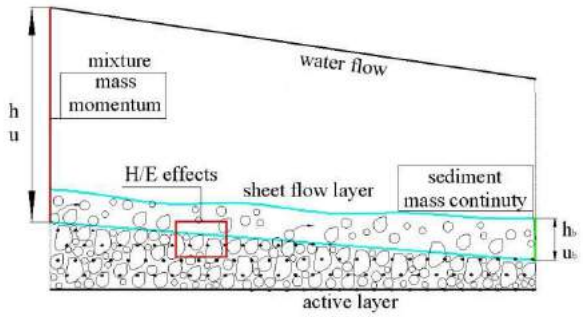

Figure 4.1: Layered flow structure composed by the bed or bottom, the transport or contact layer and the clear water layer. (Source: Guan et al., 2014).

The shallow water approach is introduced in the depth-averaging of the Navier-Stokes equations, by assuming that the horizontal length scale is much greater than the vertical length scale. Under this condition, conservation of mass implies that the vertical velocity of the fluid is small enough that it can be removed from the equation. It can be shown from the momentum equation that the vertical pressure gradients are nearly hydrostatic, and that horizontal pressure gradients are due to the displacement of the pressure surface, implying that the velocity field is constant throughout the fluid depth (Canelas et al., 2013).

The system of conservation equations is closed by equations the describe flow resistance, for particular rheologies, and bed-flow interactions.

The numerical model is then used to compute a number of well defined initial value problem with analytical solutions on a structured square mesh.

The software used to compute the numerical solutions is Matlab, which features flexible debugging

tools with graphical interfaces, allowing for real time monitoring of the simulations. Matlab also has native GPU support to allow for much faster computation, although this particular feature will not be an object of study in the current thesis.

4.2 Discretization Scheme

4.2.1 System of Conservation equations

The system of equations is comprised of total mass conservation, equation 4.1, total momentum conservation in the x and y directions, equations 4.2 and 4.3 respectively, and total conservation of the sediment mass presented in the domain, equation 4.4

$$\partial_t h + \partial_x (hu) + \partial_y (hv) = -\partial_t Z_b \tag{4.1}$$

$$\partial_t (uh) + \partial_x \left(u^2 h + \tfrac{1}{2} g h^2\right) + \partial_y (uvh) = -gh\partial_x Z_b - \frac{\tau_{b,x}}{\rho_m} \tag{4.2}$$

$$\partial_t (vh) + \partial_x (vuh) + \partial_y \left(v^2 h + \tfrac{1}{2} g h^2\right) = -gh\partial_y Z_b - \frac{\tau_{b,y}}{\rho_m} \tag{4.3}$$

$$\partial_t (C_m h) + \partial_x (C_m hu) + \partial_y (C_m hv) = -(1-p)\partial_t Z_b \tag{4.4}$$

where x, y represent the spatial coordinates, t is time, h is the depth of fluid , u is the depth-averaged velocity in the x direction, v is the depth-averaged velocity in the y direction, Z_b is the bed elevation, ρ_m is the depth averaged density of the mixture, C_m is the depth-averaged concentration of the mixture, S_x and S_y are source terms induced by second order perturbations due to stratification (Ferreira, 2005).

The term $\partial_t Z_b$ represents total bed variation and is given by:

$$(\mathbf{1} - \mathbf{p})\partial_t Z_b = \frac{(q_s - q_s^*)}{\Lambda} + \frac{1}{A}\partial_t \partial V \tag{4.5}$$

where q_s is the sediment discharge, q_s^* is the sediment discharge capacity, and λ is an adaptation length. The first term on the left side of the equation represents hydraulic erosion and the second term represents the sediment mass variations induced by the instabilization of the side slopes of the breach.

4.2.2 Finite Volume Scheme applied to the 2D Shallow-Water Equations

The system of conservation equations presented in equations 4.1, 4.2, 4.3 coupled with the Exner equation for sediment transport, can be written in form:

$$\partial_t \boldsymbol{U}(\boldsymbol{V}) + \nabla \cdot \boldsymbol{E}(\boldsymbol{U}) = \boldsymbol{H}(\boldsymbol{U}) \Leftrightarrow \partial_t \boldsymbol{U}(\boldsymbol{V}) + \partial_x \boldsymbol{F}(\boldsymbol{U}) + \partial_y \boldsymbol{G}(\boldsymbol{U}) = \boldsymbol{H}(\boldsymbol{U}) \tag{4.6}$$

where $\boldsymbol{V}$ is the vector of primitive variables, $\boldsymbol{H}$ is the vector of conservative variables, $\boldsymbol{F}$ is the flux in the vector in the x direction, $\boldsymbol{G}$ is the flux in the vector in the y direction and $\boldsymbol{H}$ is the vector of source

terms, the later of which can be subdived as $H = R + T + S$, where R expresses the friction and vertical fluxes, T represents the bottom source terms and S relates to the stratification and variation of density.

The dependent non-conservative variables in V, conservative variables in H and fluxes in F and G are:

$$\boldsymbol{V} = \begin{bmatrix} h \\ u \\ v \\ C_m \end{bmatrix}; \quad \boldsymbol{U} = \begin{bmatrix} h \\ uh \\ vh \\ C_m h \end{bmatrix}; \quad \boldsymbol{F} = \begin{bmatrix} uh \\ u^2 h + \frac{1}{2} g h^2 \\ uvh \\ C_m hu \end{bmatrix}; \quad \boldsymbol{G} = \begin{bmatrix} vh \\ vuh \\ v^2 h + \frac{1}{2} g h^2 \\ C_m hv \end{bmatrix} \tag{4.7}$$

and the source terms in R and T are:

$$\boldsymbol{R} = \begin{bmatrix} -\partial_t Z_b \\ -\frac{\tau_{b,x}}{\rho^{(w)}} \\ -\frac{\tau_{b,y}}{\rho^{(w)}} \\ -(1-p)\partial_t Z_b \end{bmatrix}; \quad \boldsymbol{T} = \begin{bmatrix} 0 \\ -gh\partial_x Z_b \\ -gh\partial_y Z_b \\ 0 \end{bmatrix}. \tag{4.8}$$

The Finite Volume Method (FVM) discretization is then obtained by integrating the system of equations 4.6 in a cell i, and the Gauss theorem is then applied to the divergence term $\nabla \cdot \boldsymbol{E}(\boldsymbol{U})$ to obtain:

$$\partial_t \int_{\Omega_i} \boldsymbol{U}(\boldsymbol{V}) dS + \oint_{\Gamma_i} \boldsymbol{E}(\boldsymbol{U}) \cdot \boldsymbol{n} dl = \int_{\Omega_i} \boldsymbol{H}(\boldsymbol{U}) dS \tag{4.9}$$

where $\boldsymbol{E} \cdot \boldsymbol{n} = \boldsymbol{F} n_x + \boldsymbol{G} n_y$ with $\boldsymbol{n} = (n_x, n_y)^T$ being the outward normal to cell Ω_i.

Assuming the representation is piecewise, and that the cell area is A_i, and performing the boundary integral on the n_i edges of the cell i, one obtains from equation 4.9:

$$\partial_t A_i \langle \boldsymbol{U}_i \rangle + \sum_{k=1}^{N} L_k \langle \boldsymbol{E} \cdot n \rangle_{ik} = A_i \langle \boldsymbol{H}_i \rangle \tag{4.10}$$

where $\langle\rangle$ represents the spatial average in the cell and L_k is the length of the k edge.

The flux variations can be expressed as a function of the conservative variables using a Jacobian matrix, orthogonal to the edge in question. Since the flux vectors are not homogeneous functions of the dependent variables, for the shallow water types system, it is usually not possible to obtain a diagonal matrix for the Jacobian for x and y directions simultaneously, thus, an approximate Jacobian matrix (Canelas, 2010; Toro, 2001) is used for the homogeneous part of the flux. The fluxes are then susceptible to be represented in a eigenvector based homogeneous system,

$$\Delta_{ik} \langle \boldsymbol{E} \cdot \boldsymbol{n} \rangle = (\langle \boldsymbol{E}_j \rangle - \langle \boldsymbol{E}_i \rangle) \cdot \boldsymbol{n}_{ik} = \sum_{n=1}^{N} \tilde{\lambda}_{ik}^{(n)} \alpha_{ik}^{(n)} \tilde{\boldsymbol{e}}_{ik}^{(n)} \tag{4.11}$$

where N denotes the dimension of the eigenspace, in this case $N = 4$ since there are three continuity equations plus one sediment conservation equation. $\tilde{\lambda}^{(n)}$ is the n eigenvalue of the system, $\alpha_{ik}^{(n)}$ are coefficients to represent wave strength and $\tilde{e}_{ik}^{(n)}$ is the n eigenvector of the edge k pointing to the exterior

of the cell i.

The averaged variables are u, v,c (velocity of small perturbations) and C_m are:

$$\tilde{u}_{ik} = \frac{u_i\sqrt{h_i} + u_j\sqrt{h_j}}{\sqrt{h_i} + \sqrt{h_j}}; \quad \tilde{v}_{ik} = \frac{v_i\sqrt{h_i} + v_j\sqrt{h_j}}{\sqrt{h_i} + \sqrt{h_j}}; \quad \tilde{c}_{ik} = \sqrt{g\frac{h_i + h_j}{2}}; \quad \tilde{C}_{m_{ik}} = \frac{C_{m_i}\sqrt{h_i} + C_{m_j}\sqrt{h_j}}{\sqrt{h_i} + \sqrt{h_j}} \tag{4.12}$$

With the average variables, the corresponding eigenvalues and eigenvectors are the calculated and given by:

$$\tilde{\lambda}^{(1)}_{ik} = (\tilde{\boldsymbol{u}} \cdot \boldsymbol{n} - \tilde{c})_{ik}; \quad \tilde{\lambda}^{(2)}_{ik} = (\tilde{\boldsymbol{u}} \cdot \boldsymbol{n})_{ik}; \quad \tilde{\lambda}^{(3)}_{ik} = (\tilde{\boldsymbol{u}} \cdot \boldsymbol{n} + \tilde{c})_{ik}; \quad \tilde{\lambda}^{(4)}_{ik} = (\tilde{\boldsymbol{u}} \cdot \boldsymbol{n})_{ik} \tag{4.13}$$

$$\tilde{\boldsymbol{e}}^{(1)}_{ik} = \begin{bmatrix} 1 \\ \tilde{u} - \tilde{c}n_x \\ \tilde{v} - \tilde{c}n_y \\ \tilde{C_m} \end{bmatrix}_{ik}; \quad \tilde{\boldsymbol{e}}^{(2)}_{ik} = \begin{bmatrix} 0 \\ -\tilde{c}n_y \\ \tilde{c}n_x \\ 0 \end{bmatrix}_{ik}; \quad \tilde{\boldsymbol{e}}^{(3)}_{ik} = \begin{bmatrix} 1 \\ \tilde{u} + \tilde{c}n_x \\ \tilde{v} + \tilde{c}n_y \\ \tilde{C_m} \end{bmatrix}_{ik}; \quad \tilde{\boldsymbol{e}}^{(4)}_{ik} = \begin{bmatrix} 0 \\ 0 \\ 0 \\ 1 \end{bmatrix}_{ik} \tag{4.14}$$

where in eq. 4.13 $\tilde{\boldsymbol{u}}$ represents the velocity vector, $\tilde{c}$ is the average small perturbation wave strength and n is the exterior normal vector to the edge.

The wave-strengths $\alpha^{(n)}_{ik}$ associated to each variable are given by,

$$\begin{aligned} \alpha^{(1)}_{ik} &= \tfrac{\Delta_{ik}\langle h\rangle}{2} - \tfrac{1}{2\tilde{c}_{ik}}\left(\Delta_{ik}\langle \boldsymbol{u}h\rangle - \tilde{\boldsymbol{u}}_{ik}\Delta_{ik}\langle h\rangle\right)\cdot \boldsymbol{n}_{ik} \\ \alpha^{(2)}_{ik} &= \tfrac{1}{\tilde{c}_{ik}}\left(\Delta_{ik}\langle \boldsymbol{u}h\rangle - \tilde{\boldsymbol{u}}_{ik}\Delta_{ik}\langle h\rangle\right)\cdot \boldsymbol{t}_{ik} \\ \alpha^{(3)}_{ik} &= \tfrac{\Delta_{ik}\langle h\rangle}{2} + \tfrac{1}{2\tilde{c}_{ik}}\left(\Delta_{ik}\langle \boldsymbol{u}h\rangle - \tilde{\boldsymbol{u}}_{ik}\Delta_{ik}\langle h\rangle\right)\cdot \boldsymbol{n}_{ik} \\ \alpha^{(4)}_{ik} &= \Delta_{ik}\langle hC_m\rangle - \tilde{C_m}\Delta_{ik}\langle h\rangle \end{aligned} \tag{4.15}$$

The numerical fluxes from **T** are discretized in the same way as the advective flux terms i.e. as a basis formed by the approximate eigenvalues (Murillo and García-Navarro, 2010). This allows the source terms in T to participate in the flux update, representing actual numerical fluxes themselves, whenever source terms are involved at the edges by means of topography variations (Canelas et al., 2013).

$$\Delta_{ik}\langle \boldsymbol{T}\cdot\boldsymbol{n}\rangle = \sum_{n=1}^{N_W} \tilde{\lambda}^{(n)}_{ik}\beta^{(n)}_{ik}\tilde{\boldsymbol{e}}^{(n)}_{ik} \tag{4.16}$$

The expressions for the eigenvalues associated to the bottom source terms are:

$$\beta^{(1)}_{ik} = -\frac{1}{2\tilde{c}_{ik}}\left(\frac{p_b}{\rho_w}\right); \quad \beta^{(2)}_{ik} = 0; \quad \beta^{(3)}_{ik} = -\beta^{(1)}_{ik}; \quad \beta^{(4)}_{ik} = 0 \tag{4.17}$$

The Finite Volume Method discretization is then completed, with $N = 4$ as the eigenspace and considering a an orthogonal quadricular matrix with equally spaced squares, $k = 4$,

$$\boldsymbol{U}_i^{n+1} = \boldsymbol{U}_i^n - \frac{\Delta t}{A_i} \sum_{k=1}^{3} L_k \sum_{n=1}^{4} \left(\tilde{\lambda}^{(n)} \alpha^{(n)} - \beta^{(n)} \right)_{ik}^{-} \tilde{\boldsymbol{e}}_{ik}^{(n)} + \Delta_t \left(R_i^{n+1} \right) \tag{4.18}$$

4.2.3 Evolution of bed morphology. Contact layer charaterization

As explained in chapter 4.1 the structure of the flow is idealized as layered domain, and sediment transport happens in the contact layer. Ferreira (2005) proposed that the thickness of the contact load layer is related to the flux of kinetic energy associated to the fluctuating motion of moving grains due to local imbalance and global equilibrium of rates of production and dissipation of fluctuating kinetic energy, i.e. the more energy is generated at the bottom of the contact load layer, the larger the thickness to allow for complete dissipation.

The interaction between the contact load layer and the bottom generate frictional stresses and collisional stresses due to sediment particle collision. If the frictional stresses and collisional stresses across the frictional sublayer are not in equilibrium, then the bed will be vertically displaced (Canelas, 2010). The rate of change of the bed elevation is a direct consequence of this non-equilibrium and is given by equation 4.5.

The sediment discharge q_s is given by:

$$q_s = C_m \mathbf{u} h \tag{4.19}$$

where C_m is the depth averaged sediment concentration, $\mathbf{u}$ is the flow velocity and h is the depth of fluid.

The equilibrium sediment discharge is given by:

$$q_s = C_c^* \mathbf{u_c} h_c \tag{4.20}$$

where C_c^* is the layer-averaged capacity concentration in the contact load layer, u_c is the contact layer depth-averaged velocity and finally h_c is the thickness of the contact layer.

The closure equation for h_c is given by the formula:

$$\frac{h_c}{d_s} = m_1 + m_2 \theta \tag{4.21}$$

where m_1 and m_2 can be considered constants for a certain range of granular material comprising sand and plastic pellets (Ferreira, 2005), and θ is the shields parameter.

The depth-averaged velocity in the contact layer was calculated by Ferreira (2005) following numerical simulation of the vertical profile of the longitudinal velocity in the contact load layer, obtaining:

$$\frac{u_c}{d_s} = u(\frac{h_c}{h})^{1/6} \tag{4.22}$$

Considering $\tan(\varphi_b)$ is the dynamic friction angle of the granular material, C_c^* is given by:

$$C_c^* = \frac{\theta d_s}{\tan(\varphi_b)} \tag{4.23}$$

The adaptation length Λ is the length necessary to retrieve capacity sediment transport downstream after a given sediment transport imbalance is imposed upstream (Ferreira, 2005) and is given by:

$$\Lambda = \frac{L_{max} - L_{min}}{\pi - |\arctan(-\theta_{ref})|} \arctan((\theta - \theta_{ref})14) + |\arctan(-14\theta_{ref})| + L_{min} \tag{4.24}$$

where L_{max} and L_{min} are the maximum and minimum adaptation lengths respectively, and are constants dependent on the significant diameter of the bottom material.

4.2.4 Closure equations for bottom friction

In the transport layer, the mixture will behave as a hyperconcentrated flow due to the sediment concentrations being high. For this type of flows, the total shear stress can be expresses as a sum of four different types of stresses (Julien and OBrien, 1997)

$$\tau = \tau_y + \tau_v + \tau_t + \tau_b + \tau_d \tag{4.25}$$

where τ_y is the yield stress, τ_v is the viscous stress, τ_b is the turbulent stress and τ_d is the dispersive stress.

The bed shear stress is given by:

$$\tau_b = C_f \rho_m u^2 \tag{4.26}$$

where C_f is the friction coefficient given by (Canelas, 2010):

$$C_f = \frac{u d_s}{h w_s} \tag{4.27}$$

where the fall velocity of the sediment particles w_s is calculated by the formula of Jimenez and Madsen (2003).

$$\begin{cases} w_s = \frac{S}{4.5} & ; S < 1 \\ w_s = \frac{S}{A + \frac{B}{S}} & ; S \geqslant 1 \wedge S \leqslant 150 \\ w_s = 1.83 & ; S \geqslant 150 \end{cases} \tag{4.28}$$

In equation 4.28 $A = 0.954$ and $B = 5.121$; $d_m = d_s/0.9$ is the normal diameter and S is the shape coefficient given by:

$$S = \frac{d_n}{4\mu} \sqrt{(s-1) g d_s} \tag{4.29}$$

4.2.5 Instabilization algorithm

A geotechnical instabilization engine was implemented to simulate the lateral widening of the breach, when a critical angle is reached for the side slopes. Figure 4.2 represents the instabilization algorithm:

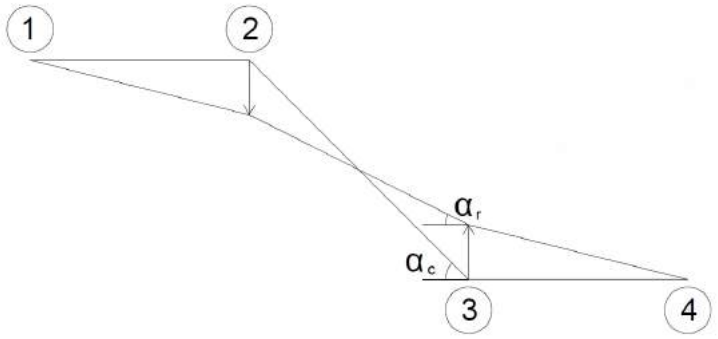

Figure 4.2: Instabilization engine for mass displacement

where α_c is the critical angle for activating the mechanism, and α_r is the residual or equilibrium angle left after the mass is displaced. The soil mass slides between two cells and remains in the domain, altering the bottom configuration.

4.2.6 Mesh generation and Matlab environment for numerical simulation

The type of mesh chosen to use in the numerical simulation is a structured two-dimensional quadrilateral mesh, composed by equally discretized squares. Choosing this type of grid allows for easier discretization and allocation of the system initial conditions, since the design of the entire mesh is only dependent on the system of coordinates. When the coordinates for the matrix are defined, the connections between points and cells are automatically defined by their index, following a simple pattern. The natural ordering of the quadrilateral elements enables the construction of very efficient numerical algorithms for solving the flow equations (Bono and Awruch, 2007).

It is also expected that the rigidity of the grid will help in the discretization of the bed morphology, since unstructured meshes can leave an artificial roughness in the bed when using non-equilibrium formulations of the shallow-water equations.

In figures 4.3 and 4.4 a graphical representation is presented of the connections in a structured grid, and looking at the indexes from the cells, cell points and sides, a clockwise patter can be found to generate each component of the grid (point, sides, cells). By mapping the connections and thus obtaining the exterior normal of each cell side, the fluxes for the numerical scheme can be easily allocated in each time step, as well as the treatment for source terms, entropy and flow velocity (see Canelas, 2010, for more information).

The software used to proceed with the numerical simulations was Matlab, a very regarded numerical simulation environment for its ability to perform debugging during each of the simulation steps, allowing the user to monitor each variable, as well as graphically represent each step of the operation.

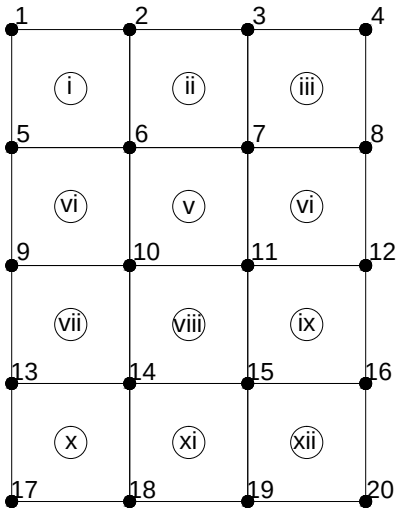

Figure 4.3: Example of mesh generation, nodes detail

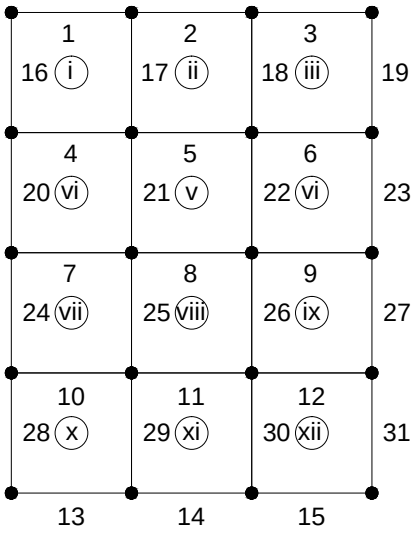

Figure 4.4: Example of mesh generation, sides detail

Mesh generation

The mesh generation and preparation involves several steps performed, summarized bellow. The initial conditions for the mesh such as length and width of the domain and sizes of the computational elements are user defined as well as the boundary conditions.

1. calculate the number of vertexes, cells and sides for the grid

2. the plane [x,y] is used to generate the coordinates of each cell barycenter with the origin of the referential in the middle of the grid.

3. generate connection matrix for each side. Associate each cell at the left and right side of a cell side. The connection matrix is made by stages since the connections of the sides on the borders will be the different. The connections for each of the four border are made, giving the same connection on the left and right side of the cell side. Then for the interior sides the connectivity is made by following each side number in the same sequence shown in figure 4.4.

4. attribute the exterior normal vector to each cell side, attending to the connection of that cell side.

5. create the topography of the problem and initial conditions. The main purpose of the toolbox will be to design a simple embankment dam with upstream and downstream slopes as well as a crest and pilot channel. Other types of geometries can be used, each of them defined by a different user created algorithm.

Chapter 5

Results

5.1 Introduction

5.2 Comparison between analytical solutions and numerical simulations

5.2.1 Dam-break test cases, initial conditions

For the dam-break test cases, the classical Stoker solution is presented and compared to the numerical model, as well as other solutions for particular cases of the Stoker solution (dry bed, discontinuous bottom elevation), with the intent to develop shocks and to verify the models ability to simulate the solution. The non-dimensional parameters that describe the initial conditions for the test cases must specify all the dependent variables (Ferreira, 2005) are for this problem:

$$\alpha = \frac{h_R + |min(0, Y_b l)|}{h_L + |min(0, Y_b l)|}; \qquad \delta = \frac{Y_b l}{h_L + max(0, Y_b l)} \tag{5.1}$$

Figure 5.1 shows a the general scheme for the initial conditions when dealing with unidimensional dam break test cases:

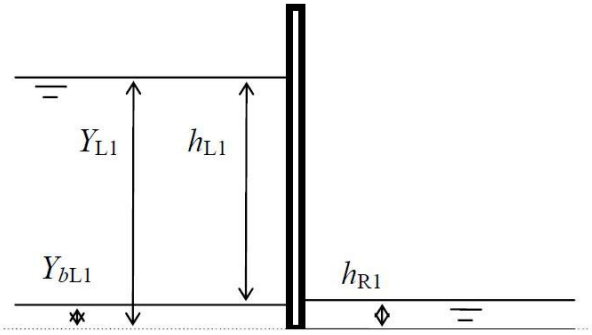

Figure 5.1: Initial conditions for 1D dam break test case

where h_R and h_L are the water heights of the initial right and left states, respectively, and $Y_b l$ is the bed elevation on the left side.

Dam-break with flat bottom. Stoker solution

This case is a particular instance of a Riemann problem, which consists of an initial value problem coupled with an initial value discontinuity. For this particular scenario a flat bed is considered and no energy gradient due to friction or turbulent stresses. The values for h_R and α are 10 and 0.1, respectively, and $\delta = 0$.

The exact solution consists of an expansion wave associated with $\gamma^-$and a shock wave. For the expansion wave associated with γ^- the solution is:

$$\begin{aligned} h &= \tfrac{1}{9g}(2c_L - \tfrac{x}{t})^2 \\ u &= \tfrac{2}{3}(c_L + \tfrac{x}{t}) \end{aligned} \tag{5.2}$$

where c is the propagation velocity of small perturbations. Considering S is the shock wave propagation speed, the Rankine-Hugoniot shock conditions express the following:

$$\begin{aligned} (h_1 - h_R)S &= (uh)_1 - (uh)_R \\ ((uh) - (uh)_R)S &= (u^2h + \tfrac{1}{2}gh^2)_1 - (u^2h + \tfrac{1}{2}gh^2)_R \\ u_1 + 2c_1 &= u_L + 2c_L \end{aligned} \tag{5.3}$$

The numerical and analytical solutions are presented in figure 5.2 using self similar[1] coordinates. In the solution presented CFL = 1, no friction is regarded, and quadrilateral structured mesh is used, with sides measuring 0.005 m. Both the analytical and computational solutions are presented for $t = 1.0$ s.

[1] For a problem withouth dimensions this technique consists to find by inspection all the dilations that do not change the equation and the boundary conditions (Lagrée)

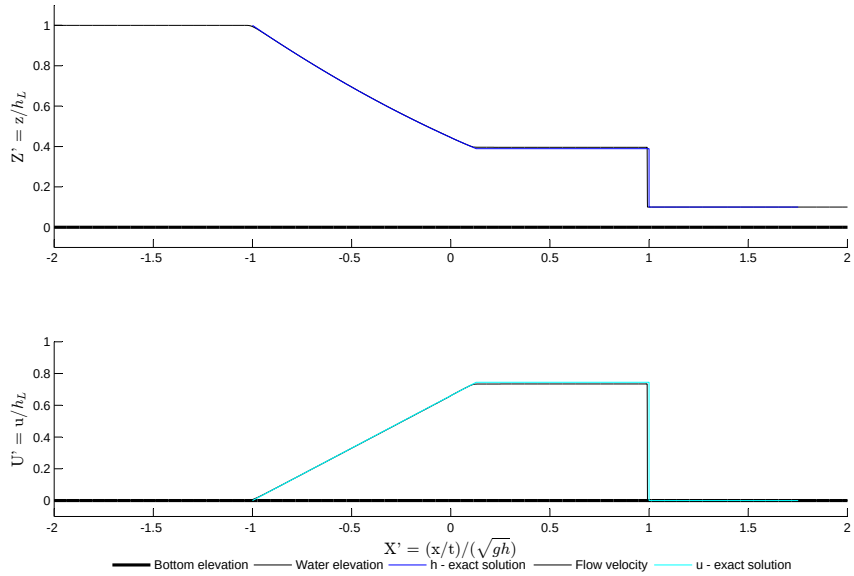

Figure 5.2: Comparison between analytical and numerical solution of the Stoker problem

Figure 5.2 shows a clearly the left moving expansion wave and right moving shock wave. The figure also shows a good accordance between the computed and exact solution for the problem presented.

Dam-break with flat bottom. Ritter solution

The Ritter solution is a particular case for the Stoker solution, when $h_R = 0$ i.e. in a dry bed scenario. The solution for the shock wave speed expressed in 5.3 becomes:

$$\begin{aligned} \lim_{h_R \to 0} S &= \lim_{h_R \to 0} \frac{(uh)_1 - (uh)_R}{h_1 - h_R} = u_1 \\ \lim_{h_1 \to 0} u_1 &= \lim_{h_R \to 0} 2(c_L - c_1) = 2c_L \end{aligned} \tag{5.4}$$

therefore the solution becomes simple and is the expansion wave expressed, for which the profile is given by equation 5.2.

For the the conditions $h_L = 10.0$ m, $\alpha = 0.0$, $\delta = 0.0$ and $CFL = 1.0$, the solution is computed against the analytical solution, with the same mesh used to compute the Stoker solution and the results are shown in figure 5.3 for $t = 1.0$ s

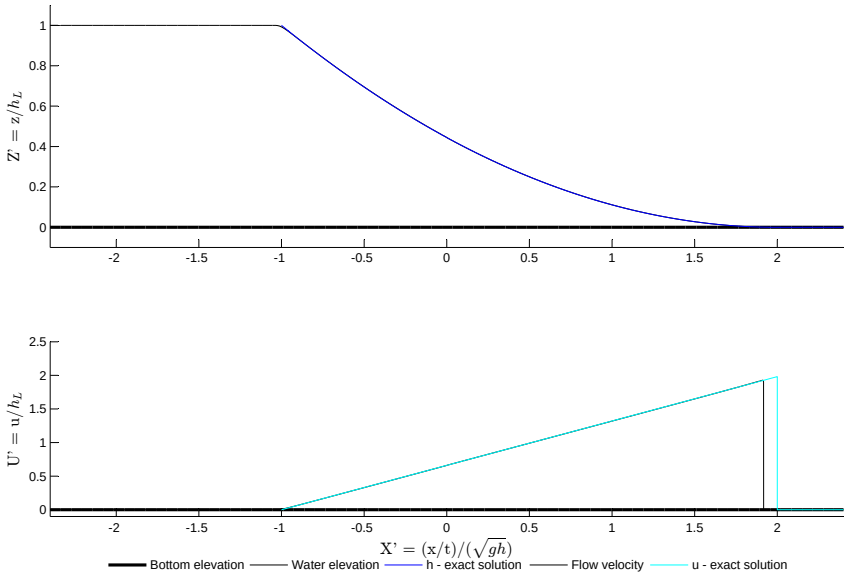

Figure 5.3: Comparison between analytical and numerical solution of the Ritter problem

A delay is seen between the two solutions, as well as a decreased shock speed magnitude, this reveals the dissipative nature of the numerical scheme, which will be explored more in the following problems.

The correct behavior of the wetting front is observed and also a good agreement between the analytical and computational solution. Taking from the results in Canelas (2010) the denser mesh provides a better comparison, and with an even denser mesh, it is possible to converge to the exact solution.

5.2.2 2D test cases

In this section initial value problems are simulated and compared with the respective analytical solutions. The first two are circular dam problems, which are a 2D generalization of the 1D dam break problems presented before, and the solutions are the same since the 2D solution has radial symmetry with the 1D solution.

Cirucular dam break. Dry bottom

The dry bottom circular dam break is also a radial generalization of the Ritter solution i.e. for a circular water column with $1.0\ \mathrm{m}$ and $\alpha = 0$, $\delta = 0.0$ the exact solution is the same as for the unidimensional case.

The numerical solution is presented in figure 5.4 in self similar coordinates, for a computational domain of 20000×20000 discretized as 100×100 cells and $CFL = 1.0$.

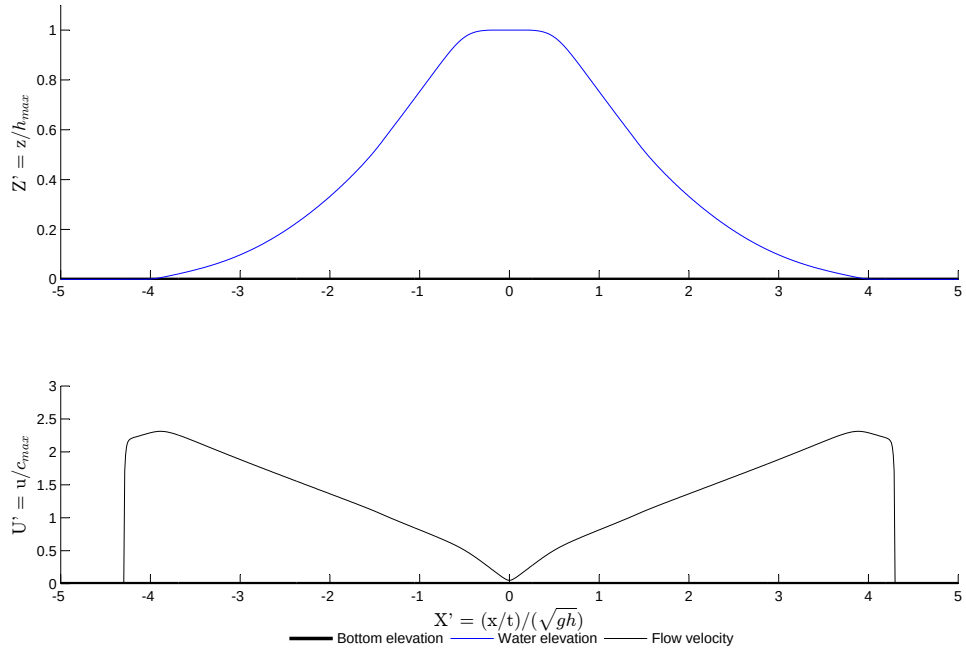

Figure 5.4: Circular dam-break problem simulation for water and velocity profiles, $t = 1s$

Comparing the 2D and 1D solutions it is observed that the behavior is the same, as expected. The numerical solution also shows the influence of the mesh density in the agreement between numerical and analytical solutions since for the numerical scheme the velocity profile is smoother and the peak is eliminated. For a denser mesh, the peak is more noticeable as show for the unidimensional case.

The 3D water profile and velocity map are also presented in figures 5.5 and 5.6 respectively

where the radial symmetry is observed. Inn the velocity magnitude field the effects of the orthogonal mesh are also observed, in the form of velocity peaks in the principal directions x and y. These peaks

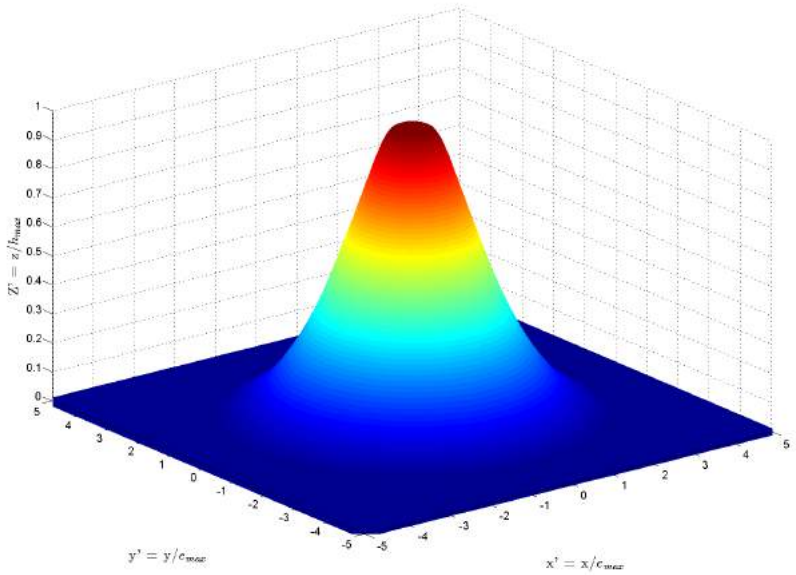

Figure 5.5: 3D perspective of the water profile, $t = 1\ \mathrm{s}$

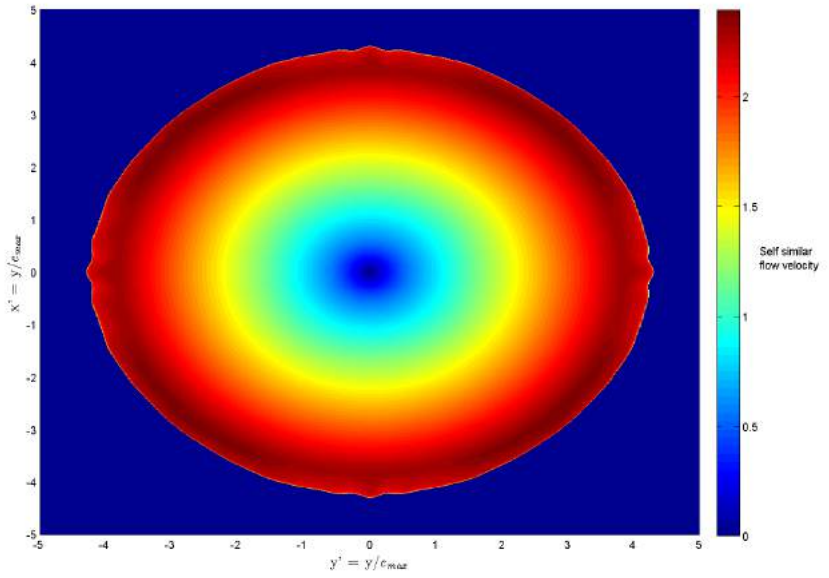

Figure 5.6: 2D flow velocity map, $t = 1\ \mathrm{s}$

appear as a result of the structured quadrilateral mesh chosen to represent the domain, where the sides of the cells are always parallel or perpendicular to the directions x and y of the referential.

5.2.3 Water movement in parabolic basin

The problems presented in the following section where proposed by Thacker (1981) and exact solutions for different initial conditions where derived from the shallow water equations. The general formulation of the problem is presented in Appendix A.

There are two particular cases for the geometry of the basin presented:

$$D = D_0(1 - \frac{x^2}{L^2} - \frac{y^2}{l^2}) \tag{5.5}$$

where in equation 5.5, D_0 is depth at the center of the basin, and L and l are the distance from the center of the basin to the shoreline in the x and y direction respectively.

The first is for $l = L$ rendering the basin a parabola of revolution, the other is for $L \ll l$, creating a cylindrical channel. Only the first particular case will be considered for the following solutions of the nonlinear shallow-water wave equations.

Oscilations for which the surface remains planar

Assuming that for the general equations presented in equation A.6 and A.7, $u_x = u_y = v_x = v_y = 0$, leading to $h_{xx} = h_{yy} = hxy = h_{yx}$, only u_0, v_0 and h_0 define the initial conditions of the motion. For basins studied, consider $f = 0$.

Consider ω the frequency of the motion, the complete solution for the motion is (Thacker, 1981) :

$$\begin{gathered} u = -\nu\omega\sin(\omega_1 t); \quad v = -\nu\omega\cos(\omega_1 t) \\ h = 2\nu\tfrac{D_0}{L}(\tfrac{x}{L}\cos(\omega_1 t) - \tfrac{y}{L}\sin(\omega_1 t) - \tfrac{\nu}{2L}); \\ \omega_1 = (\tfrac{2gD_0}{L^2})^2 \end{gathered} \tag{5.6}$$

where ν determines the amplitude of the motion.

The shoreline is determined by equation 5.7,

$$(x - \nu\cos(\omega_1 t))^2 + (y + \nu\sin(\omega_1 t))^2 = L^2 \tag{5.7}$$

where the moving shoreline is a circle in the x, y plane and the motion is such that the center of the circle orbits the center of the basin (Thacker, 1981).

The initial profile of the analytical solution is shown in figure 5.8 for $t = T/8$ and the full 3D domain is presented in figure 5.7.

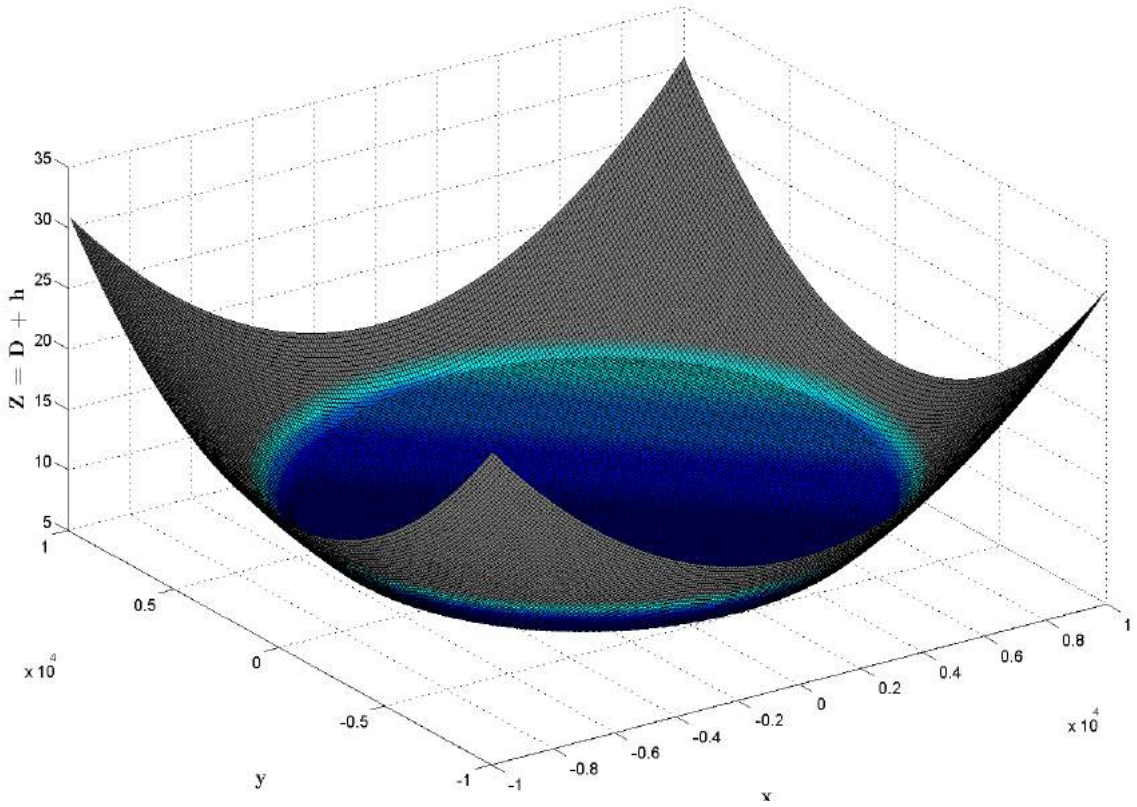

Figure 5.7: Initial water profile, 3D view. $t_0 = T/8$

The discretization scheme considered was a 20000×20000 domain discretized as 100×100 cells and $CFL = 0.8$.

The results and comparison of the numerical and analytical solutions for $t = T/8$, $t = T/2$, $t = 3T/4$, $t = T$ are presented in figure 5.9

From the analysis of images a) to d) it is observed that the numerical model behaves as expected, and the surface of the water stays planar, showing a good agreement with the analytical solution. Once again the effects of the mesh density are evidenced, since over time a fictional viscosity resulting from the dissipative nature of the numerical scheme, slows the flow, relative to the exact solution.

A probe was placed inside the domain, on the point $(x, y) = (-4050, -50)$ to monitor the water surface variation over time, as well as the flow velocity u and v. The results are presented in figure 5.10 for a time period of $\Delta t = 8400$ s.

The velocity profiles u and v for $t = T$ is also shown in figures 5.11 and 5.12.

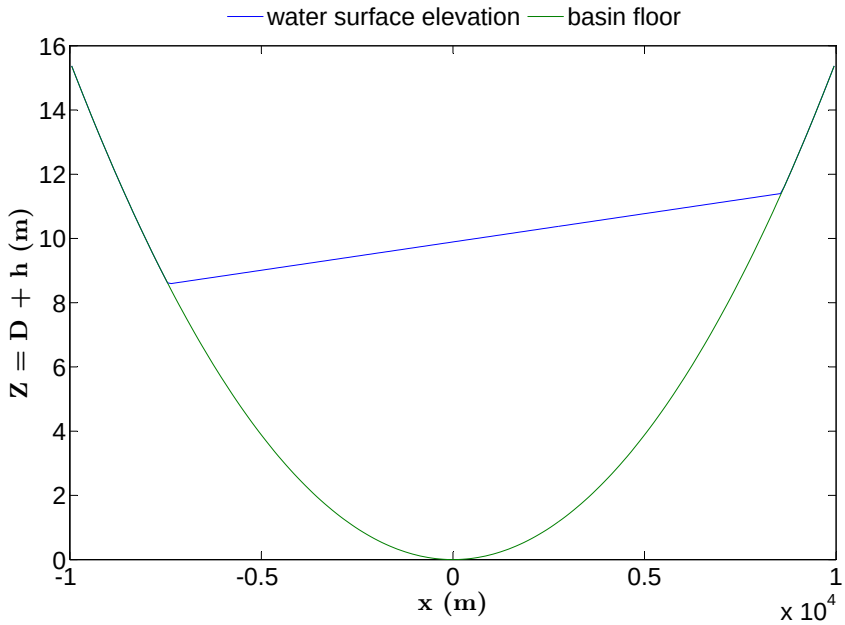

Figure 5.8: Initial water profile, 2D view. $t_0 = T/8$

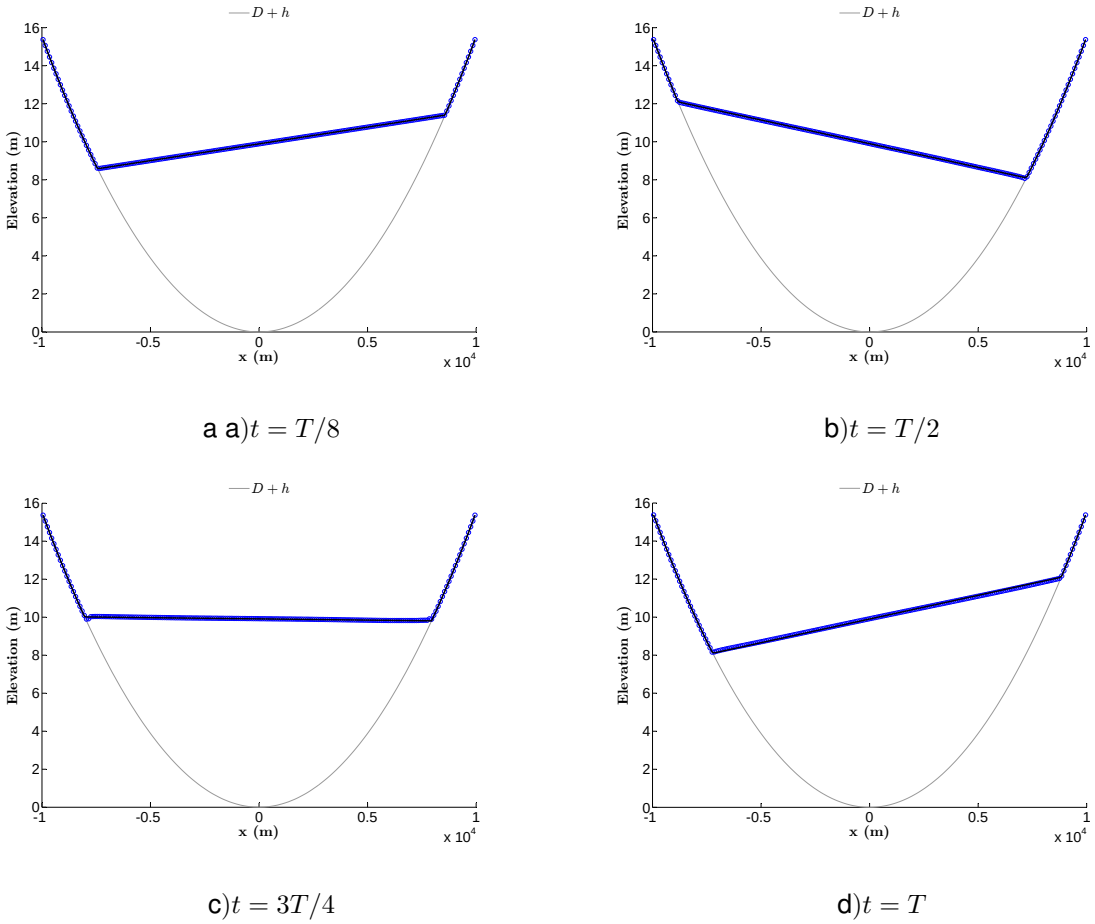

a a)$t = T/8$ b)$t = T/2$

c)$t = 3T/4$ d)$t = T$

Figure 5.9: Water surface elevation in different instants, comparison with analytical solution

Oscilations for which the surface is curved

Now assuming that $u_0 = v_0 = 0$, restricting the motion to convergence toward, divergence from, and rotation about the center of the basin. For a this particular case,$f = 0$, $h_x = h_y = 0$, $u_x = v_y$ and

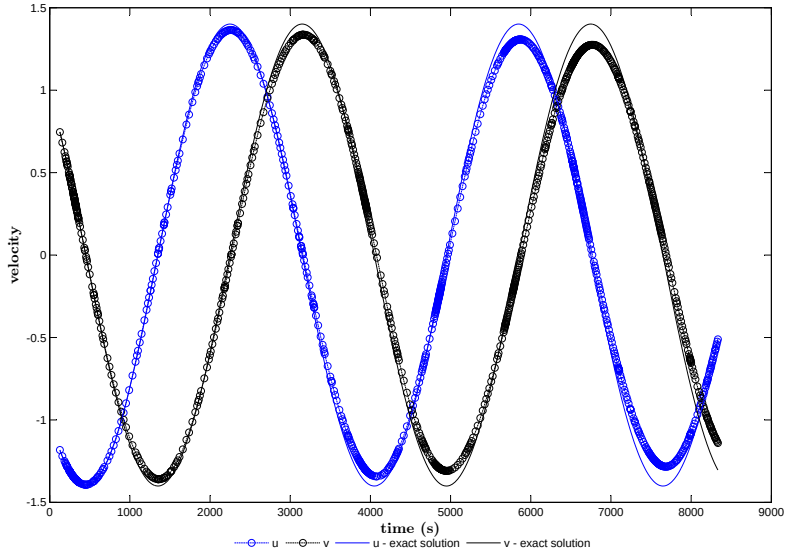

Figure 5.10: Variation of u and v over time for probe 1 $(x, y) = (-4050, -50)$. Comparison with analytical solution

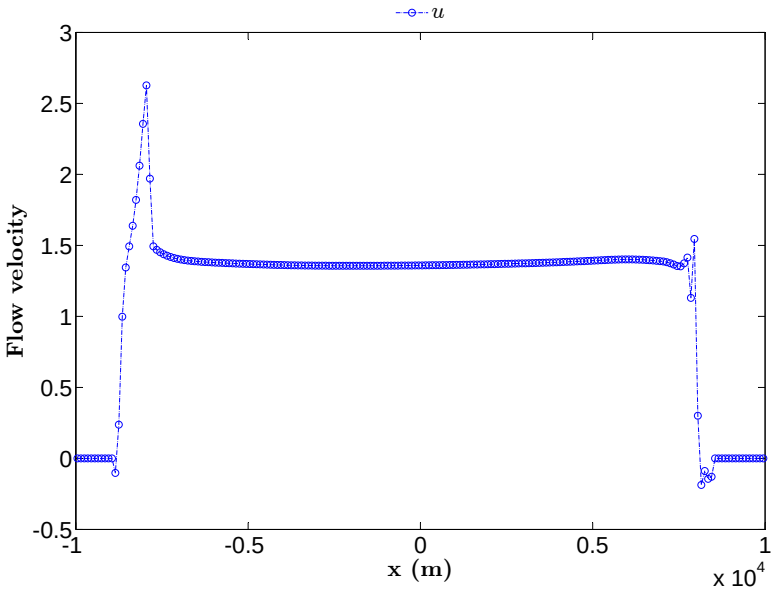

Figure 5.11: Longitudinal profile of u velocity field for $t = 2200$ s

$u_y = -v_x$, the seven initial conditions presented in Appendix A are reduced to three and are calculated by equations 5.8

$$\begin{aligned} &\frac{\delta^2 u_x}{\delta t^2} + u_x \frac{8gD_0L^2}{+} 6u_x \frac{\delta u_x}{\delta t} + 4{u_x}^3 = 0; \\ &\frac{\delta v_x}{\delta t} + 2u_x v_x = 0; \\ &\frac{\delta h_0}{\delta t} + 2u_x(h_0 + D_0) = 0 \end{aligned} \tag{5.8}$$

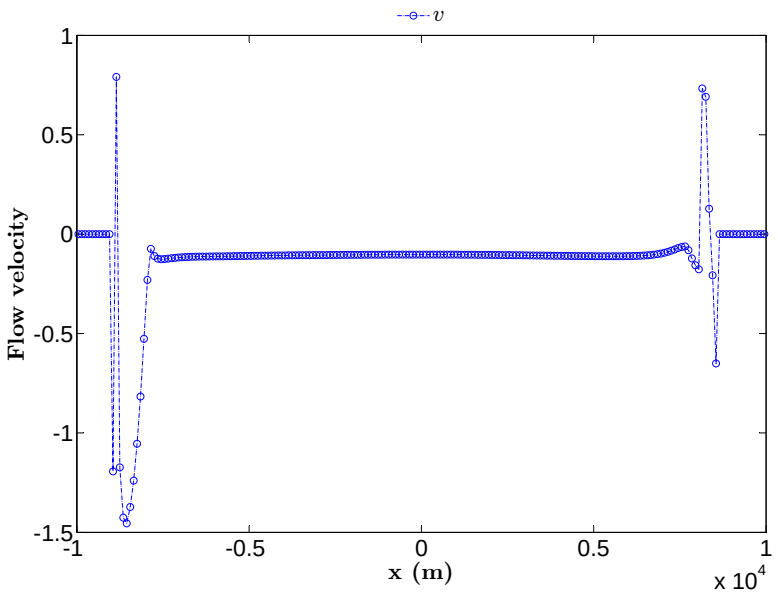

Figure 5.12: Longitudinal profile of v velocity field for $t = 2200$ s

the initial value of v_x is v_{x0} and the inital value of h is ν. Considering that u_x is initially zero, the complete solution for the motion becomes (Thacker, 1981):

$$\begin{aligned} u &= \tfrac{1}{1-A\cos(\omega t)}[\tfrac{1}{2}\omega(x)A\sin(\omega t) + A(\cos(\omega t) - 1)]; \\ v &= \tfrac{1}{1-A\cos(\omega t)}[\tfrac{1}{2}\omega(y)A\sin(\omega t) + A(\cos(\omega t) - 1)]; \\ h &= D_0\{\tfrac{(1-A^2)^{\frac{1}{2}}}{1-A\cos(\omega t)} - 1 - \tfrac{x^2+y^2}{L^2}[\tfrac{1-A^2}{1-A\cos(\omega t)} - 1]\}. \end{aligned} \tag{5.9}$$

where A is a constant that depends on values v_{x0} and ν and is calculated by equation 5.10:

$$A = \frac{(D_0+\nu)^2 - {D_0}^2}{(D_0+\nu)^2 + {D_0}^2} \tag{5.10}$$

the frequency of the motion ω is given by equation 5.11

$$\omega^2 = \frac{8gD_0}{L^2}; \tag{5.11}$$

The initial profile of the water surface is a parabola of revolution and the profile is presented in figures 5.13 and 5.14 for the instant $t = 0$ s. The parameters used the same for the previous problem, and are also expressed in table .....

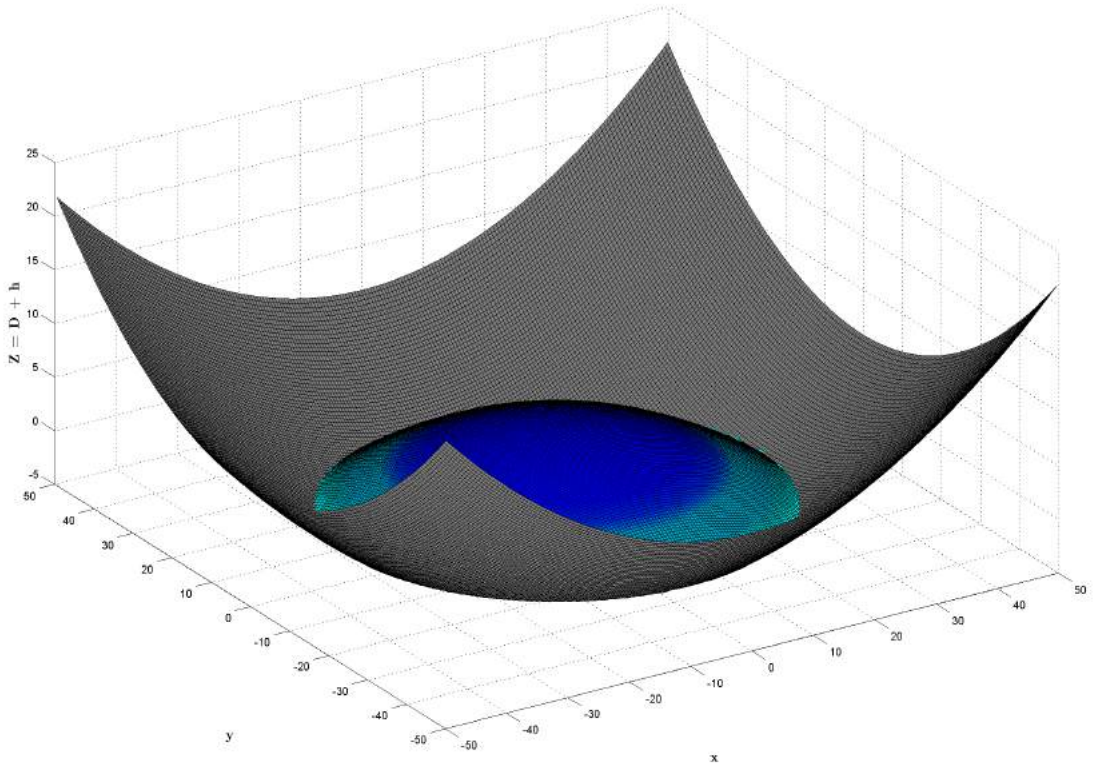

Figure 5.13: Initial Water elevation, 3D view, $t = 0$

The motion of the water in the parabolic basin is such the shoreline is a circle with a variable radius that expands and contracts as the central water elevation is above or beow the equilibrium level, creating a convex or concave water surface respectively. This induces multiple wetting and drying situations across the domain, providing a very good test for model stability under the conditions presented.

The analytical and numerical solutions for the motion are presented in figure 5.14 corresponding to the instants $t = 0$, $t = T/4$, $t = T/2$, $t = 3T/4$.

where a good agreement between the analytical and numerical solutions is observed. It is also noted that a the amplitude of the motion is dampened over time, due to the drying algorithm, which leaves a thin layer of water in the domain, for model stability purposes (Kurganov and Petrova, 2008). This causes a dissipation of the total momentum. Further analysis and remodeling of the wetting and drying algorithm should be considered in order to preserve the total momentum.

The same problem is also evident when analyzing the data collected by the probes, placed at the same locations as the previous problem. Probe data is presented in figure 5.15 for probe 1 and figure 5.15 for probe 2.

The dampening caused by the mesh induced viscosity is more noticeable for the velocity in the x

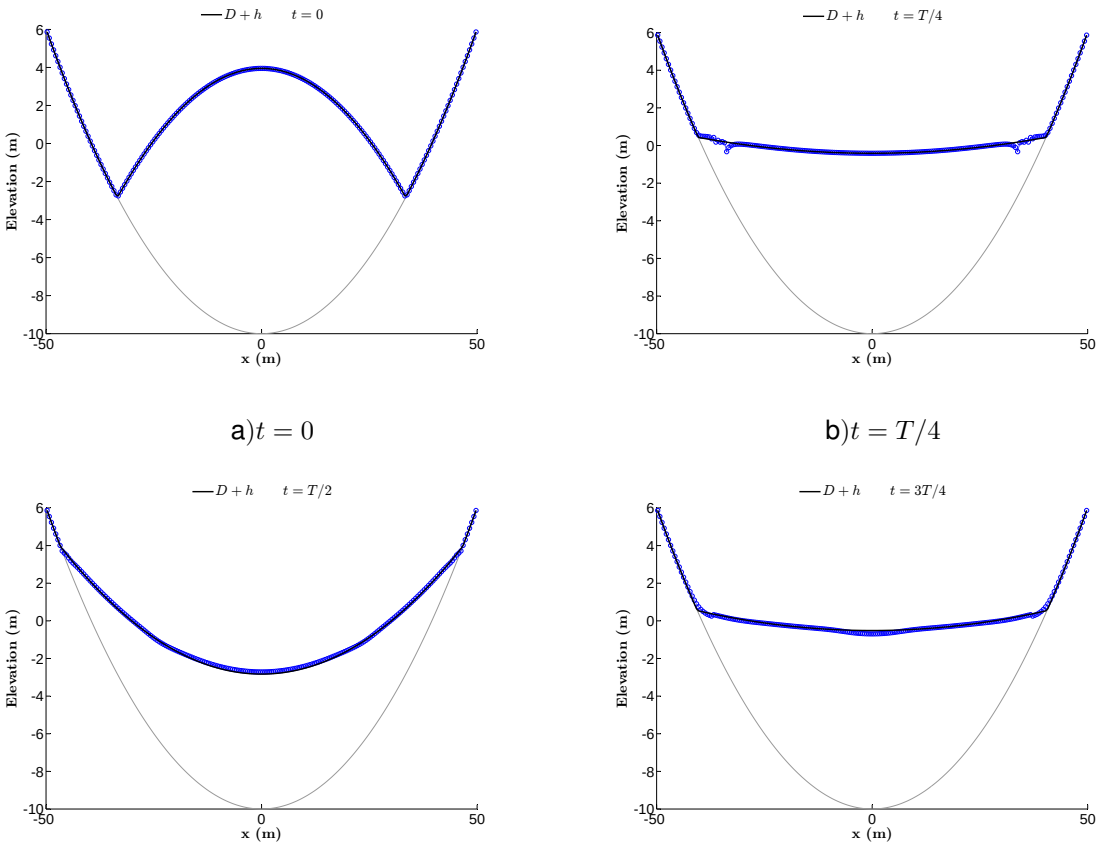

a)$t = 0$ b)$t = T/4$

c)$t = T/2$ d)$t = 3T/4$

Figure 5.14: Water surface elevation in different instants, comparison with analytical solution

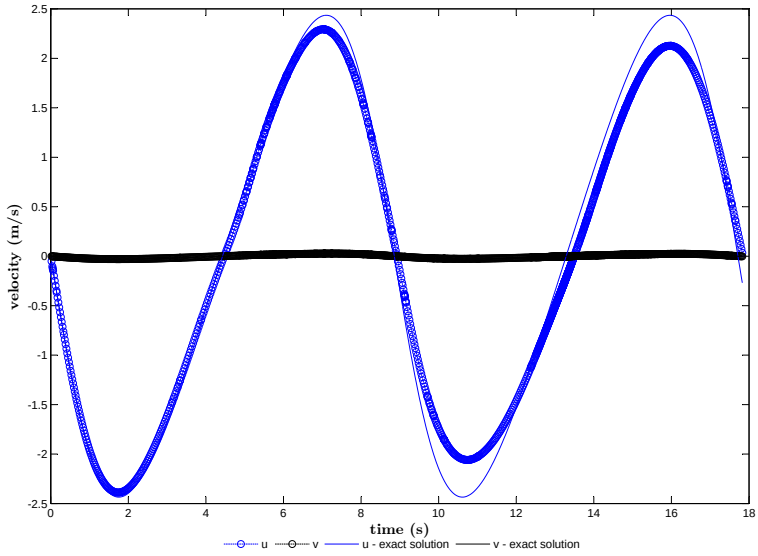

Figure 5.15: Data for u and v collected in probe 1, comparison with analytical solution

direction, u. The drying conditions are also observed in figure 5.16, but although the probes starts with $h = 0$, when the probe is drying, there is always a small layer of water, caused by the drying conditions and accentuated by the rundown of the water that was halted by this algorithm at higher elevations.

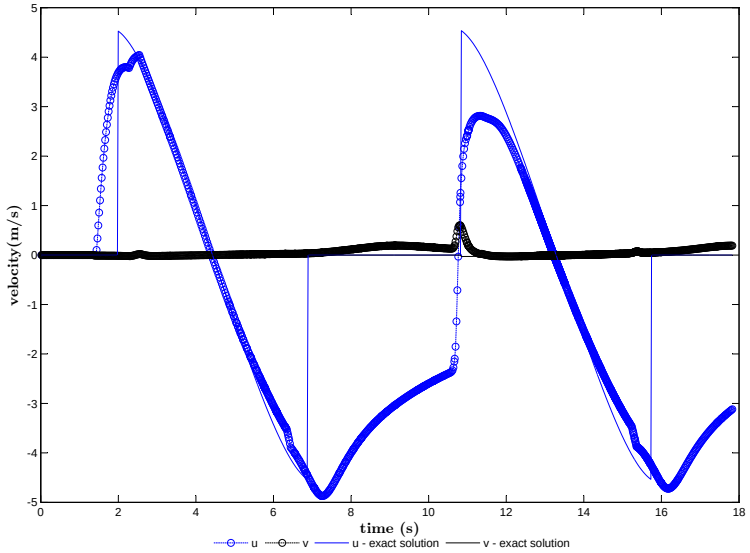

Figure 5.16: Data for u and v collected in probe 2, comparison with analytical solution

To conclude the analysis of the drying conditions, a three dimensional map for the velocity in the x direction is presented. Note that the velocity peaks of the velocity map correspond to cells where water was previous stoped and is now flowing down the domain walls.

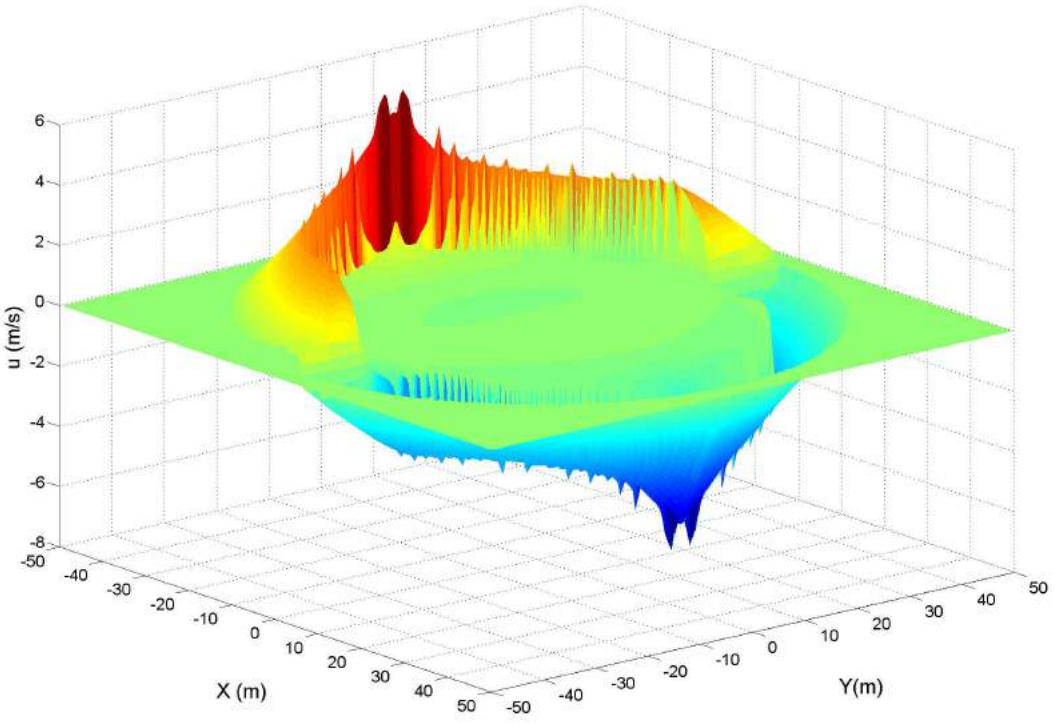

Figure 5.17: 3D view of the u velocity profile $t = T$

5.2.4 Mobile bed. Riemann problems

Initial conditions

The previous problems where developed to test model accuracy and stability in frictionless and non erodible beds. The conceptual model features sediment mass conservation, and the purpose of the numerical model is to simulate situations where dam breaching is expect, a phenomena characterized by the complex erosion mechanisms as explained in chapter 2. The governing equations where presented in chapter 4 and the following chapter will focus on some of the theoretical solutions for the Riemann problem with the full set of equations of conservation for mass, momentum and sediment mass.

The problems are presented in the form of dam breaks, which can be idealized as instantaneous removal of a vertical barrier initially separating two constant states that extend indefinitely on both up- and downstream directions. If this description is valid, then the problem is a Riemann problem and admits self-similar solutions if the system of governing hyperbolic equations is homogeneous (Ferreira, 2005).

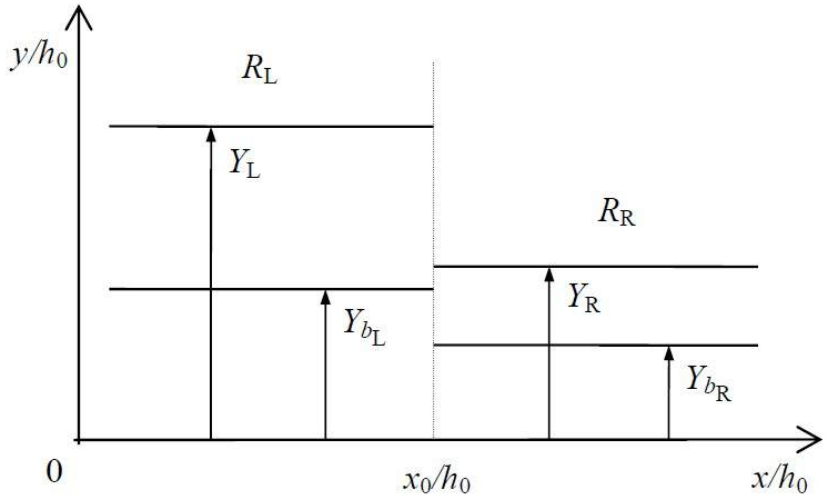

Figure 5.18: Initial conditions for the Riemann problem posed to the geomorphic shallow water equations

In figure 5.18 the initial conditions are presented.The variables, Y_L, Y_L, R_R, R_R, Yb_L and Yb_R are the water elevation, the unit mass discharge and the bed elevation for the left (L) and right (R) constant states separated by the initial discontinuity.

The solution of comprised of a combination of expansion and shock waves associated with the first three characteristics γ^1, γ^2 and γ^3 and the general structure of the solution is presented in figure 5.19.

Analytical solution for the Riemann problem

Two types of problem were considered, using the same non-dimensional parameters as in section 5.2.1. No flow resistance is considered to obtain the theoretical solution, and the sediment concentration law is:

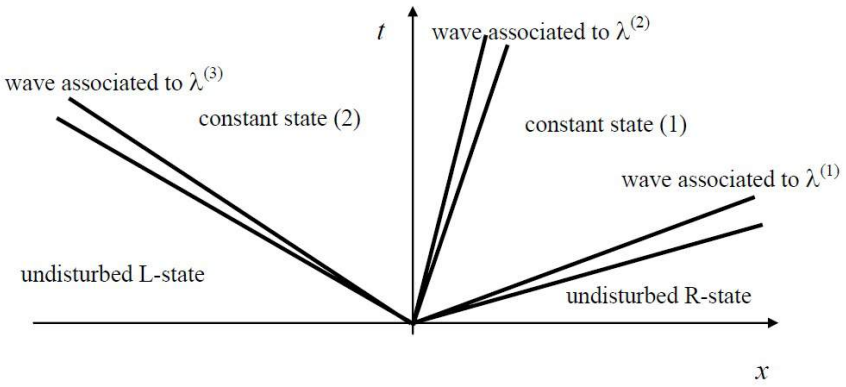

Figure 5.19: General wave structure of the Riemann solution for the geomorphic dam-break problem.

$$C = a_c u^2 h^{-1}. \tag{5.12}$$

where a_c is the mobility coefficient. No flow resistance is considered to obtain the analytical solution.

The two different types of problem are presented in table 5.1 along with the initial conditions considered for each of the four problems analyzed.

Solution	h_L [m]	h_R [m]	Y_{bL} [m]	Y_{bR} [m]	a_c	d_s[m]	s
Type A	0.40	0.00	0.00	0.00	0.0010142	0.003	1.5
	0.40	0.00	0.00	0.10	0.0010142	0.003	1.5
Type B	0.40	0.10	0.08	0.00	0.0010142	0.003	1.5
	0.40	0.10	0.00	0.08	0.0010142	0.003	1.5

Table 5.1: Initial conditions for the 2 types of solution for the geomorphic dam break problem

Solutions of type A problems are comprised of two rarefaction waves associated with $\gamma^{(3)}$ and $\gamma^{(2)}$ and one shock wave associated with $\gamma^{(1)}$ characteristic. The 7×7 system of equations the describe the solution of the problem is:

$$(Y_R - Y_1)S_1 = (uh)_R - (uh)_1;$$

$$(R_R - R_1)S_1 = (\rho_m u^2 h)_R - (\rho_m u^2 h)_1 + g * \tfrac{1}{2}((\rho_m h^2)_R - (\rho_m h^2)_1) + g * \tfrac{1}{2}((\rho_m h)_R + (\rho_m h)_1)(Y_{bR} - Y_{b1});$$

$$[((1-p)Y_b + Ch)_R - ((1-p)Y_b + Ch)_1]S_1 = (Cuh)_R - (Cuh)_1 \tag{5.13}$$

$$\begin{aligned} \tfrac{\delta u}{\delta h} &= f_u{}^{(2)}(u_1, h_1); \\ \tfrac{\delta Y_b}{\delta h} &= f_z{}^{(2)}(u_1, h_1); \end{aligned} \tag{5.14}$$

$$\frac{\delta u}{\delta h} = {f_u}^{(3)}(u_2, h_2);$$
$$\frac{\delta Y_b}{\delta h} = {f_z}^{(3)}(u_2, h_2); \tag{5.15}$$

where C is the depth-averaged sediment concentration of the flow and ρ_m is the depth-averaged volumetric mass of the flow, the index 1 and 2 indicate the corresponding constant states. Equations 5.14 and 5.15 are systems of 2×2 ODE's the describe the expansion waves across the associated characteristic. Equation 5.14 requires the boundary conditions $u_0 = u_L$, $h_0 = h_L$ and $Y_{b0} = Y_{bL}$, $h_0 = h_L$ to the point $h = h_2$

Solutions of type B problems feature a similar solution structure to Type A problems, but with a shock wave associated with $\gamma^{(2)}$, and therefore must verify the Rankine-Hugoniot shock conditions, so equations 5.14 are replaced by :

$$(Y_1 - Y_2)S_2 = (uh)_1 - (uh)_2;$$
$$(R_1 - R_2)S_2 = (\rho_m u^2 h)_1 - (\rho_m u^2 h)_2 + g * \tfrac{1}{2}((\rho_m h^2)_1 - (\rho_m h^2)_2) + g * \tfrac{1}{2}((\rho_m h)_1 + (\rho_m h)_2)(Y_{b1} - Y_{b2});$$
$$[((1-p)Y_b + Ch)_1 - ((1-p)Y_b + Ch)_2]S_2 = (Cuh)_1 - (Cuh)_2 \tag{5.16}$$

The analytical solutions Type A problems are presented in figures 5.20 and 5.21.

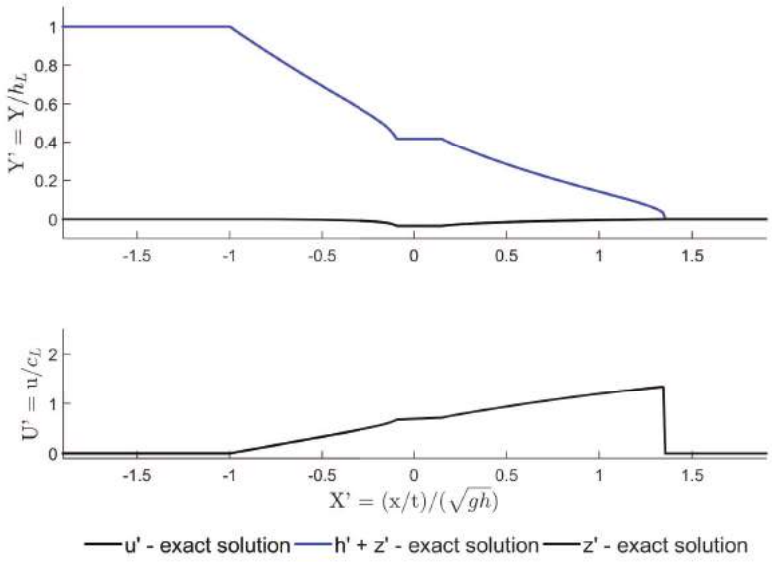

Figure 5.20: Analytical solution for Type A - problem 1

The 2 expansion waves associated with the $\gamma^{(3)}$ and $\gamma^{(2)}$ characteristics appear well defined and separated by a constant state downstream of the negative expansion wave. The shock wave is also presented, although almost negligible due to the dry initial state of the bed, which is a similar response to the Ritter solution. The bed profile responds to the variations of the water profile.

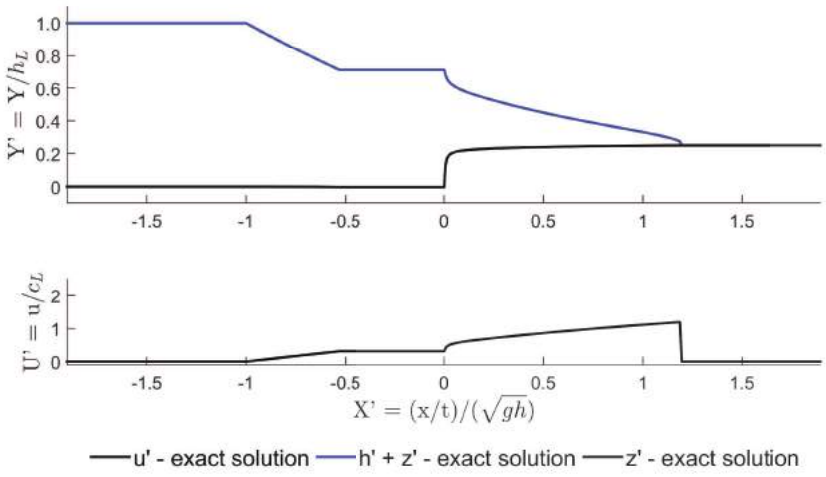

Figure 5.21: Analytical solution for Type A - problem 2

Analytical solutions for problems of Type B are also presented in figures 5.22 and 5.23.

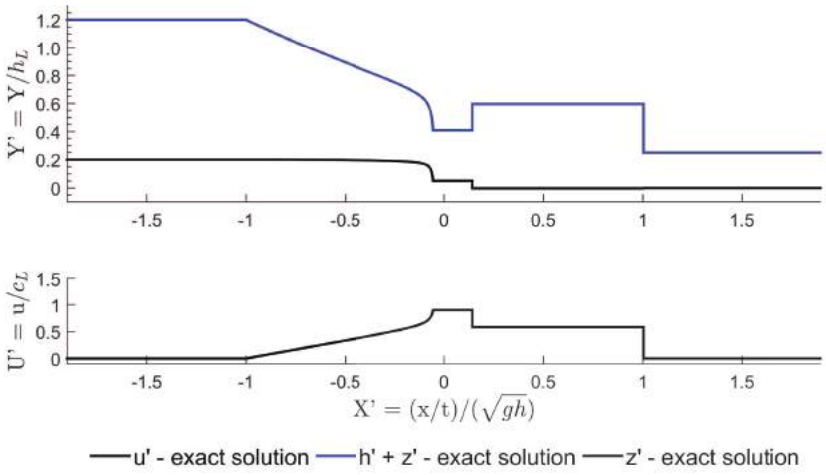

Figure 5.22: Analytical solution for Type B - problem 3

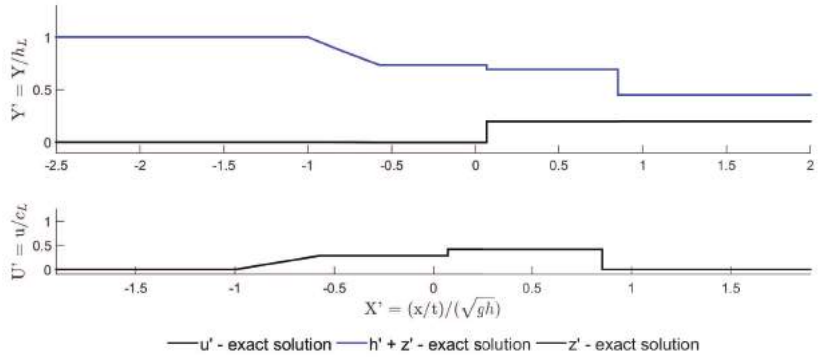

Figure 5.23: Analytical solution for Type B - problem 4.

As expected the solutions admit a shock wave associated to the $\gamma^{(1)}$ with a velocity higher than the shock associated with the $\gamma^{(2)}$ characteristics field, thus verifying the RH shock conditions.

Comparison between numerical and analytical solutions

The numerical solutions were obtained for the same conditions as the analytical solution, i.e. featuring no flow resistance, and a the same sediment discharge law. The adaptation length was taken sufficiently small to ensure a quasi-equilibrium state for sediment continuity, but with an adaptation length higher than the mesh size to ensure model stability.

For Type A problems the comparison between numerical and analytical solutions are presented in figures 5.24 and 5.25. Problems 1 and 2 feature $CFL = 0.9$ and for $t = 1$ s. Problem 1 was simulated with a 0.05×0.05 mesh and Problem 2 with a 0.005×0.005 mesh.

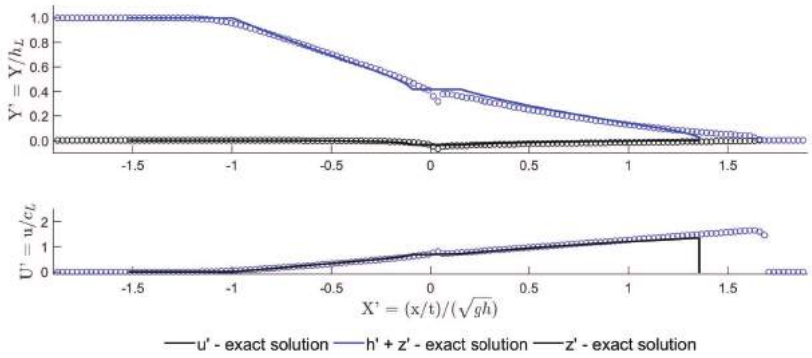

Figure 5.24: Results for numerical simulation of Problem 1, solution for water surface and bottom elevation and velocity profile. Comparison with analytical solution

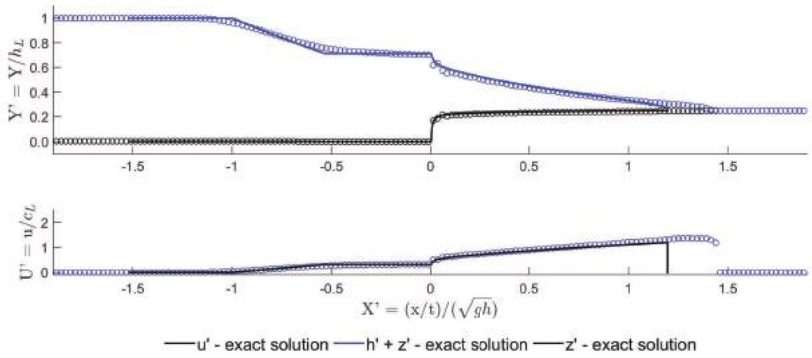

Figure 5.25: Results for numerical simulation of Problem 2, solution for water surface and bottom elevation and velocity profile. Comparison with analytical solution

Analysis of the simulations shows that erosion levels have similar magnitudes, and the bottom evolution is in good agreement with the analytical solution. The shock induced by the bottom source terms is inevitable at the end of the negative expansion wave (Ferreira et al., 2006). The numerical scheme has difficulties in simulating the wave front. The simulations provided are a good simulation of the complex dam break problem.

For the type B problems, numerical and analytical solutions are presented in figures 5.24 and 5.25. Problems 3 and 4 feature $CFL = 0.9$ and for $t = 1$ s. Problem 3 was simulated with a 0.05×0.05 mesh

and Problem 4 with a 0.01×0.01 mesh.

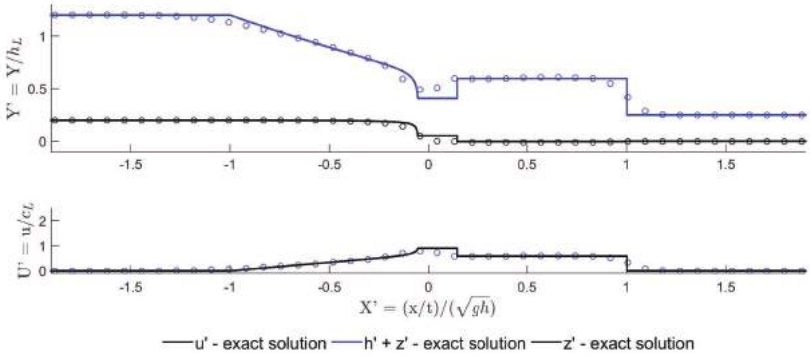

Figure 5.26: Results for numerical simulation of Problem 3, solution for water surface and bottom elevation and velocity profile. Comparison with analytical solution.

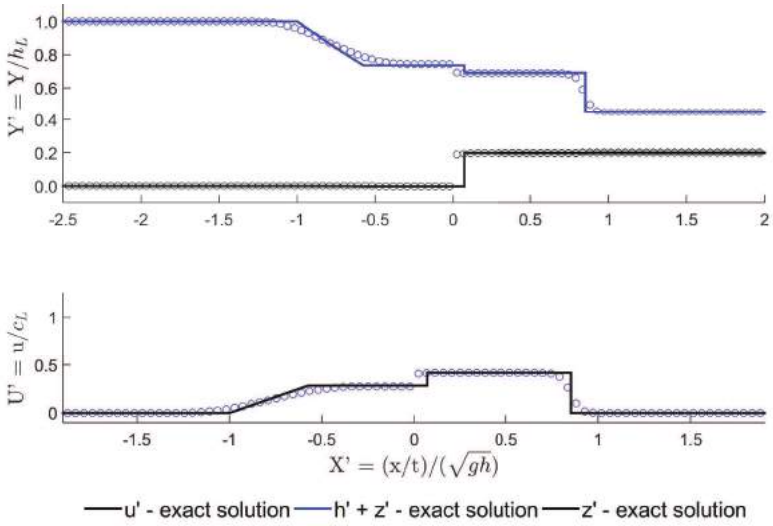

Figure 5.27: Results for numerical simulation of Problem 4, solution for water surface and bottom elevation and velocity profile. Comparison with analytical solution.

The profile of the solutions is in good agreement and the shocks are well defined, although the magnitude of the shock associated with the $\gamma^{(2)}$ characteristics field is lower in the numerical solution. The location of the shocks are very close, while showing similar bed elevation values.

5.2.5 Simulation of dam breach and comparison with experimental work

The main goal of this work is to provide a numerical model capable of simulating the breaching of embankment dams, hence, a simulation of the experimental work is now presented and the results from both the numerical model and experiments are compared. The model is equipped with an instabilization engine, applied in similar way than the ones showed in chapter 2.2. This is a very simple approach to the complex physics involved in the sliding failure that occurs during the breaching process, and for future work, a more complex instabilization engine should be developed.

Simulation results and comparison

A simplified version of the dam presented in the experiments is now modeled and the breaching is simulated. The simulated embankment features similar characteristics to the embankment used in trial 2, and this parameters are presented in table 5.2

Z_{max} [m]	$i_{upstream}$ [m]	$i_{downstream}$ [m]	L_{crest} [m]	ilot channel [	s	d_s [mm]	p
0.50	0.35	0.50	0.20	0.10	2.40	0.35	0.44

Table 5.2: Numerical model, embankment characteristics

The 3D rendering of the dam is also presented in figure 5.28

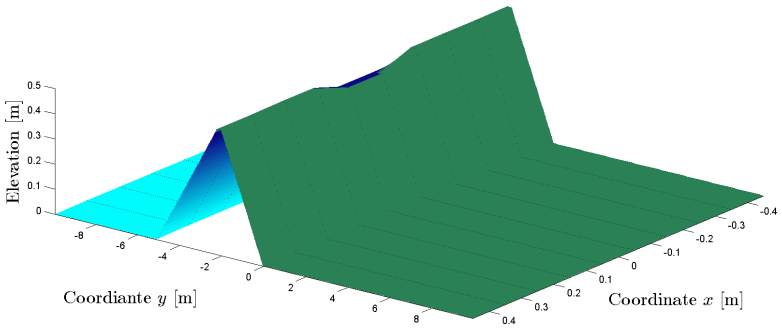

Figure 5.28: Numerical model, embankment geometry

The domain is composed of $W = 10 \times L = 10$ cm cells. The water that flow trough the breach is collected at a reservoir downstream, and the water is put back in the domain, upstream of the breaching zone, distributed over an are, as to not disturb the area near the breach.

The final breaching hydrograph is then obtained and compared with the one from trial 2, and the comparison is presented in figure 5.29:

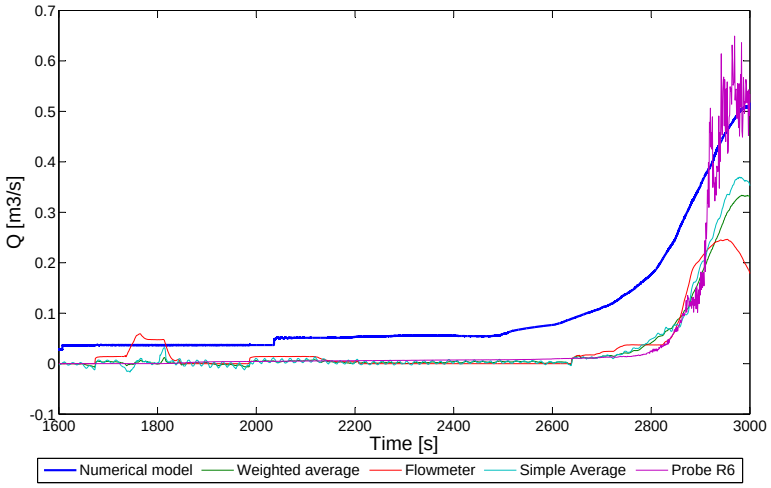

Figure 5.29: Comparison between numerical and experimental outflow hydrographs for trial 2

The peak discharge is able to be reached for the numerical model, and the evolution of the discharge is similar do the experimental results, showing a good agreement between numerical and experimental work, for very similar embankment characteristics. Note that the hydrograph evolution is smoother, because the instabilization engine does not consider sudden breach enlargements, and thus it takes longer to reach the peak. This confirms the need for further work and development of a geotechnical instabilization algorithm that can reproduce the sliding of mass due to undercutting.

Figure 5.31 shows a comparison of an upstream view of the breaching process for the experiments and for the numerical model.

The images show that the model can simulate the breaching process of an earth dam. There is also clear influence of the mesh detail, although the mesh size was chosen for computational efficiency, since a more detailed mesh would lead to infeasible computational times.

To note that the instabilization algorithm can in fact reproduce a collapse of the breach sides, but in a very different way than the observed in the experiments. The collapse is taken as an interaction between two cells, and it is clear from the image analysis that the mass displacement should not be a sequential event, and should be modeled in a more complex way.

The bottom elevations for 2 time frames of the breaching process are presented in figures 5.32 and 5.33.

The bottom profile in the numerical model shows a good agreement with the observed in the experiment. It is noticeable that more definition is needed in the proximity of the breach for a better characterization of the bottom evolution.

The water surface contours are presented for the same instant in figures 5.34 and 5.35

Similarities are evident on both water surface maps and the same definition problem is posed, but despite this the water elevation is in good agreement with the experimental data as the water profile

$t = 2747s$

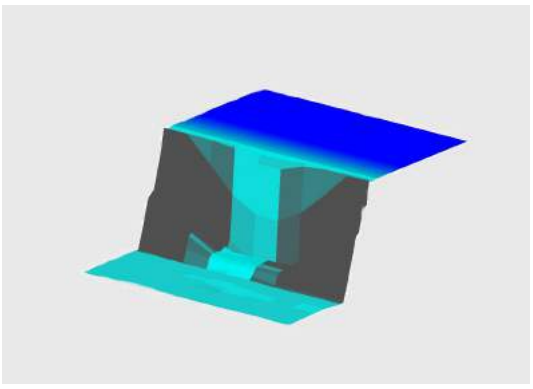

$t = 2747s$

$t = 2854s$

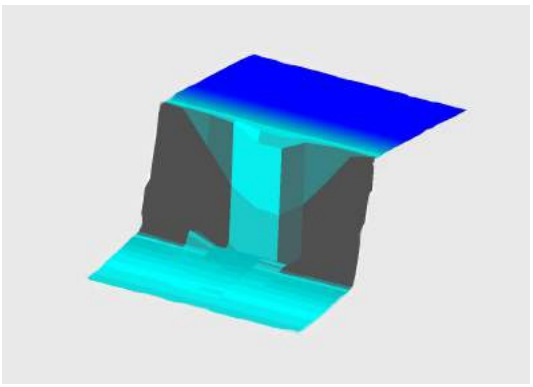

$t = 2854s$

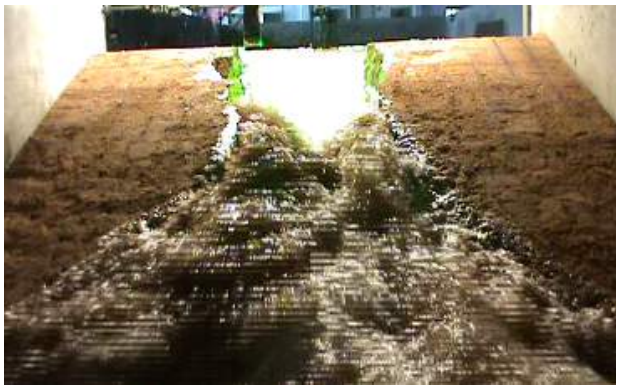

$t = 2833s$

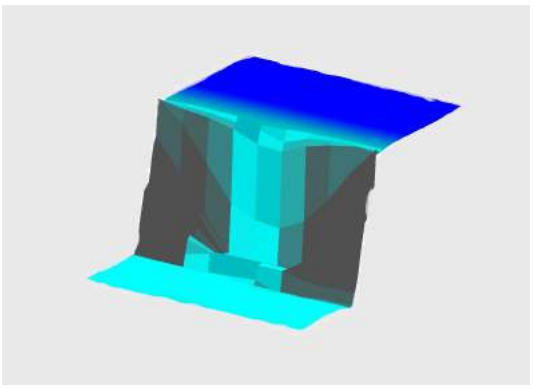

$t = 2833s$

Figure 5.30: Water surface elevation in different instants, comparison with numerical solution

contours follow a similar path.

$t = 2961s$

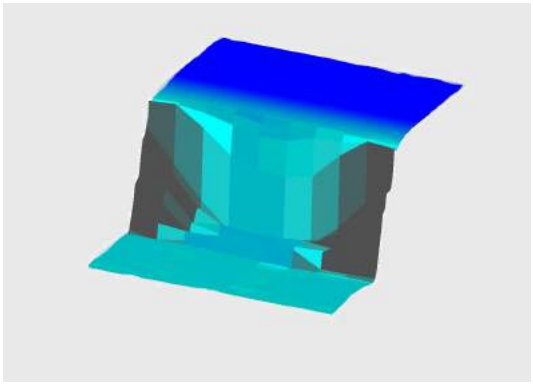

$t = 2961s$

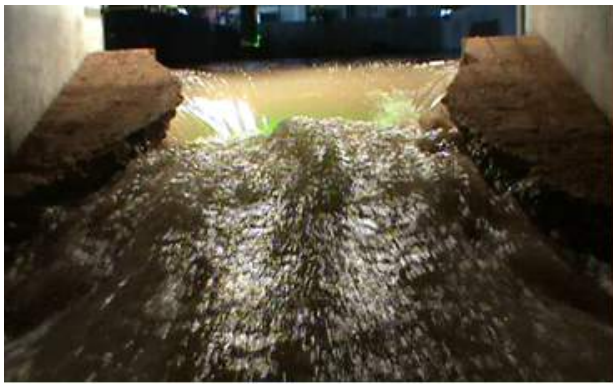

$t = 3017s$

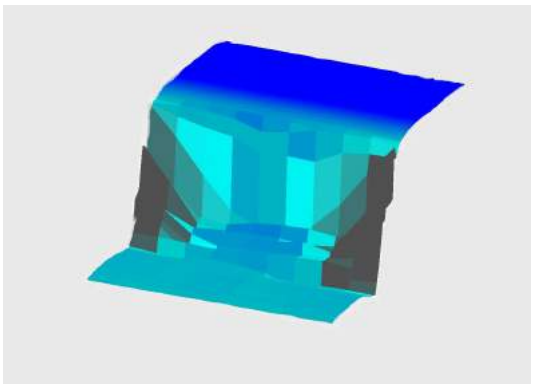

$t = 3017s$

Figure 5.31: Water surface elevation in different instants, comparison with analytical solution

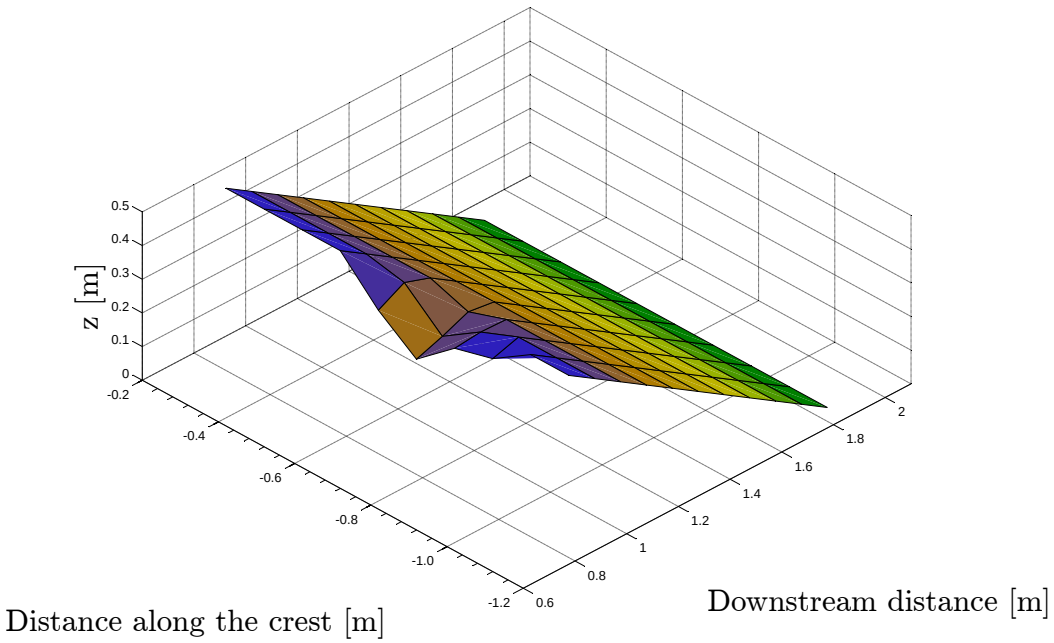

Figure 5.32: Bottom elevation for the upstream view of the embankment, numerical model.

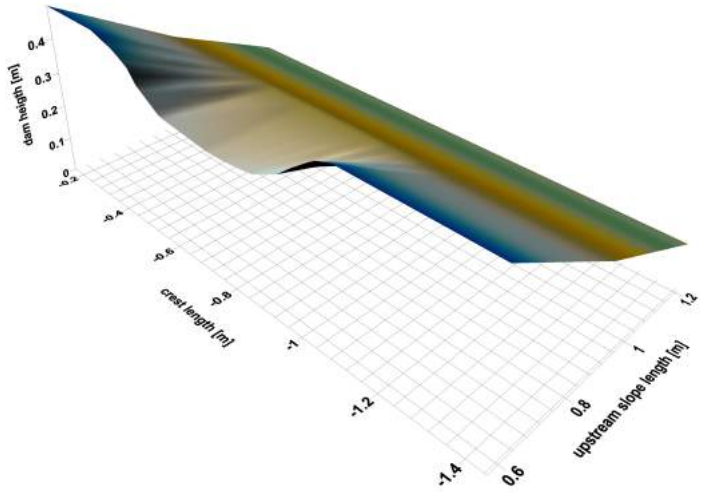

Figure 5.33: Bottom elevation for the upstream view of the embankment, experiment 2

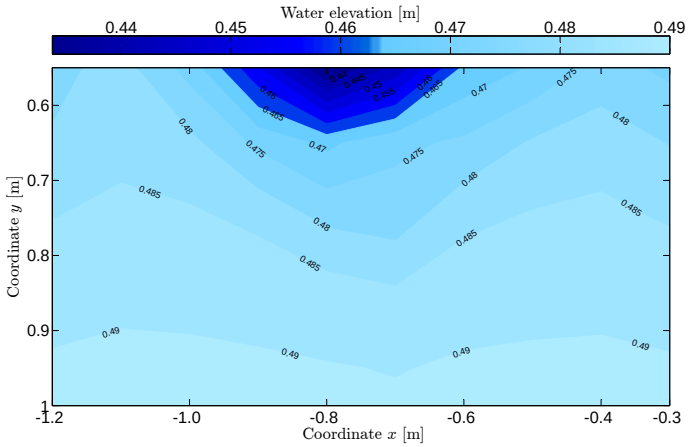

Figure 5.34: Water Surface contours for the simulation of experiment 2.

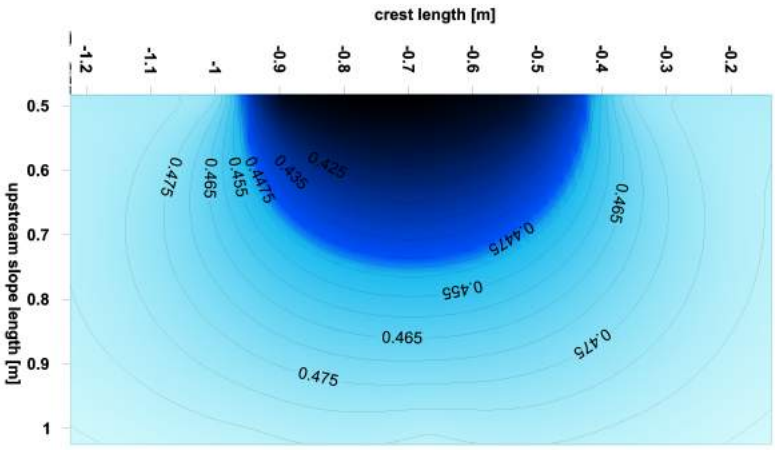

Figure 5.35: Water Surface contours for experiment 2.

Chapter 6

Conclusions

In this work, an effort to simulate the breaching process of dams was undertaken. A numerical model was developed using a simple high-level language, MATLAB, meant to become the core of a toolbox. It is envisaged that a dam-breach MATLAB toolbox would be subjected to a wide interest in the water resources community thus contributing to advance the confidence of users in deterministic tools to estimate breach hydrographs.

The conservation equations are essentially the shallow water equations complemented with mass conservation equations and a bed morphology equation. The model features non-equilibrium sediment transport. The closure equations were taken from existing literature on fluvial transport and sheet-flow (intense bedload transport) studies. The discretization method, drawn from previous studies Canelas et al. (2013), is fully conservative, robust and obeys C-property.

The model, named STAVBreach, as a upgraded installment of the model used by Canelas et al. (2011), was validated with one-dimensional and two-dimensional solutions of the shallow water equations with and without sediment transport. The agreement between the simulations and the theoretical results was satisfactory. In particular, the conservation equations proved to be able to describe the water movement and the bed configuration for several well-known cases with analytical solutions.

However, some problems were detected, mostly in the numerical discretization approach. The problems proposed by Thacker for water movement in parabolic basins with flat and curved surfaces posed some difficulties on the simulations, due to the multiple wetting and drying fronts, as well as evident mesh rigidity observed. The Riemann problems consisting of geomorphic dam breaks with variations on the water level and bottom elevations revealed that the numerical scheme has trouble simulating the shock waves celerity and propagation as well as defining the constant state due to the non-equilibrium nature of the sediment transport equations used. The scheme was confirmed to be somewhat dissipative. Additionally some problems were in what concerns the rigidity imposed by the quadrangular mesh.

Experiments conducted at a medium-scale laboratory facility at LNEC provided data for a more complex validation phase. Outflow hydrographs, determined from two different methods, were obtained as well as data for characterization of the breaching process.

The instabilization conceptual model employed to describe the mass detachment phenomena observed at the banks of the pilot channel proved to be satisfactory but not ideal. The enlargement os the breach sides was correctly modeled but with artificial values of geotechnical parameters. It is clear that the instabilization phenomena needs to be described with more detail, namely with the inclusion of three-dimensional phenomena such as undercutting, in order to be able to simulate the sudden breach enlargements observed in the experiments.

6.1 Future Work

Some recommendations and ideas for future work are proposed in this chapter:

- The is still work to be done in implementing the code as a MATLAB toolbox in order for it to be used effectively but end users.
- A revision of the numerical scheme is needed, and a higher order scheme should be developed in order to avoid excessive numerical diffusion;
- Further analysis and validation of the geotechnical instabilization model should be done, considering coupling with, well known and well studied slope instabilization numerical models, whenever possible.
- An alternative wetting and drying algorithm should be considered to mitigate the effects that current one has, especially when drying occurs in steep slopes.
- The model is explicit and heavily dependent on problem scale for computational efficiency, so for the future, graphical processing of the data should be implemented to improve simulation efficiency in order to simulate large periods of time in detailed domains.
- Different structured cells should be experimented since the square orthogonal mesh was able to simulate the problems without a significant loss of detail, and a much larger gain of efficiency, if coupled with some suggestions already made.
- Pre- and post-processing to become a proper toolbox for MATLAB.
- Include coding for GPU to improve computational performance, again to become a MATLAB toolbox.

Bibliography

Alonso, E. (2004). Suelos compactados en la teoria y en la prática.

Alonso, E. and N. Pinyol (2008). Unsaturated soil mechanics in earth and rockfill dam engineering. In D. . G. . Toll, C. . E. . Augarde, D. . Gallipoli, and S. . J. . Wheeler (Eds.), *Proceedings of the 1st European Conference, E-UNSAT 2008*. Taylor and Francis Group.

A.M. Bento, et al. (2014). *Quantification of the breach hydrograph of homogeneous dams subjected to overtopping*.

ASTM. D698. standard test methods for laboratory compaction characteristics of soil using standard effort 12 400 ft-lbf/ft3 600 kn-m/m3. west conshohocken (pa): Astm international; 2011.

Bono, G. and A. M. Awruch (2007). *Numerical study between structured and unstructured meshes for Euler and Navier-Stokes Equations*. Mecanica computacional Vol XXVI.

Caldeira, L. (2001). *Curso de exploração e segurança de barragens*. Instituto da Água.

Canelas, R. (2010). *2D Mathematical Modeling of Discontinuous Shallow Sediment-laden Flows*. Ph. D. thesis, Instituto Superior Técnico.

Canelas, R., J. Murillo, and R. Ferreira (2011). 2d simulation of discontinuous shallow flows. In *Experimental Methods in Hydraulic Research*, pp. 141–153. Springer.

Canelas, R., J. Murillo, and R. M. Ferreira (2013). Two-dimensional depth-averaged modelling of dam-break flows over mobile beds. *Journal of Hydraulic Research 51*(4), 392–407.

Cardoso, R. (2010). *Earth fill works*. Instituto Superior Técnico.

Emelen, S. V., Y. Zech, and S. Soares-Frazão (2015). Impact of sediment transport formulations on breaching modelling. *Journal of Hydraulic Research 53*(1), 60 – 72.

Ferreira, R. M., S. Amaral, J. Leal, and B. Spinewine (2006). Discontinuities in geomorphic dam-break flows. In J. L. R.M.L. Ferreira, E. Alves and A. Cardoso (Eds.), *River Flow 2006*, Volume 2, pp. 1521–1530. Taylor and Fancis Group.

Ferreira, R. M. L. (2005). *River Morphodynamics and Sediment Transport - Conceptual Model and Solutions*. Ph. D. thesis, Instituto Superior Técnico.

Guan, M., N. G. Wright, and P. A. Sleigh (2014). 2d process-based morphodynamic model for flooding by noncohesive dyke breach. *Journal of Hydraulic Engineering 140*(7).

INC., M. (2011). *Soil Compaction Handbook*. P.O.Box 6524, Carson, CA 90749: MULTIQUIP INC.

Jimenez, J. A. and O. S. Madsen (2003). A simple formula to estimate settling velocity of natural sediments. *Journal of Waterway, Port, Coastal, and Ocean Engineering 129*(2), 70–78.

Julien, P. and J. OBrien (1997). On the importance of mud and debris flow rheology in structural design. In C. L. Chen (Ed.), *Debris-Flow Hazards Mitigation: Mechanics, Prediction and Assessment*. ASCE.

Kurganov, A. and G. Petrova (2008). A central-upwind scheme for nonlinear water waves generated by submarine landslides. In *Hyperbolic Problems: Theory, Numerics, Applications*, pp. 635–642. Springer.

Lagrée, P. Self similar solutions.

Marcelino, J. (2008). *Projecto, construção e exploração de pequenas barragens de aterro*. LNEC.

Murillo, J. and P. García-Navarro (2010). Weak solutions for partial differential equations with source terms: application to the shallow water equations. *Journal of Computational Physics 229*(11), 4327–4368.

Narita, K. (2000). *Design and construction of embankment dams*. Aichi Institute of Technology.

NEVES, E. d. (2002). Algumas considerações sobre a mecânica de enrocamentos. *Solos e Rochas, Revista Latino-Americana de Geotecnia, ABMS/ABGE 25*(3), 161–203.

Parra, M. A. and J. C. C. Barranco (2003). Dams from the roman era in spain: analysis of design forms. In *Proceedings of the First International Congress on Construction History: Madrid, 20th-24th january 2003*, pp. 243–257. Instituto Juan de Herrera.

Pickert, G., G. H. Jirka, A. Bieberstein, and J. Brauns (2004). Experiments on overtopped homogeneous embankments: Soil/water interactions and breach development. In *Proc. Int. Conf. - Disasters and Society - From Hazard Assessment to Risk Reduction*. Karlsruhe.

Pickert, G., V. Weitbrecht, and A. Bieberstein (2011). Breaching of overtopped non-cohesive river embankment controlled by apparent cohesion. *Journal of Hydraulic Research 4*, 143 – 156.

RSB (2007). Regulamento de segurança de barragens.

Santos, J. (2015). Experimental investigation of failure by overtopping of homogeneous earth dams. Master's thesis, Instituto Superior Técnico.

Silva, S. (2001). Dams: What They Are and What They Do.

Singh, V. P. (1996). *Dam Breach Modeling Technology*, Volume 17 of *Water Science and Technology Library*. Kluwer Academic Publishers.

Spinewine, B., A. Delobbe, L. Elslander, and Y. Zech (2004). Experimental investigation of the breach growth process in sand dikes. In *Proceedings of the River Flow 2004*, pp. 983–991. Taylor and Francis Group.

Swartenbroekx, C., S. Soares-Frazão, R. Staquet, and Y. Zech (2010). Two-dimensional operator for bank failures induced by water-level rise in dam-break flows. *Journal of Hydraulic Research 48*(3), 302–314.

Thacker, W. C. (1981). Some exact solutions to the nonlinear shallow-water wave equations. *Journal of Fluid Mechanics 107*, 499 – 508.

Toro, E. (2001). *Shock-Capturing Methods for Free Surface Shallow Flows*. Wiley.

Volz, C., P. Rousselot, D. Vetsch, R. Mueller, R. Faeh, and R. Boes (2010). Numerical modeling of dam breaching processes due to overtopping flow. In *Proceedings of the 8th ICOLD European Club symposium*, pp. 691–696. Innsbruck,.

Zhao, G., Y. Ren, P. J. Visser, and W. S. J. Uijttewaal (2013). Flow process of the embankment breaching. In *Proceedings of 2013 IAHR World Congress*.

Appendix A

Water movement in parabolic basins, general formulation

In case an appendix if deemed necessary, the document cannot exceed a total of 100 pages...

Some definitions and vector identities are listed in the section below.

A.1 General case

The formulation of the shallow water wave equations in shallow basins is the following:

$$\begin{aligned} \tfrac{\delta u}{\delta t} + u\tfrac{\delta u}{\delta x} + v\tfrac{\delta u}{\delta y} - fv + g\tfrac{\delta h}{\delta x} = 0; \\ \tfrac{\delta u}{\delta t} + u\tfrac{\delta v}{\delta x} + v\tfrac{\delta v}{\delta y} + fu + g\tfrac{\delta h}{\delta y} = 0; \\ \tfrac{\delta u}{\delta t} + \tfrac{\delta}{\delta x}[u(D+h)] + \tfrac{\delta}{\delta y}[v(D+h)] = 0. \end{aligned} \tag{A.1}$$

In A.1 the first 2 equations describe the the variation of the velocity components u and v, and the third equations is the continuity equation. f is the Coriolis parameters which accounts for the earth's rotation and g is the gravity acceleration.

The approach taken was to assume the existence of solutions for u and v in the form:

$$u = u_0 + u_x x + u_y y; \quad v = v_0 + v_x x + v_y y. \tag{A.2}$$

requiring the solution for h to have the following form:

$$h = h_0 + h_x x + hyy + \frac{1}{2}h_{xx}x^2 + \frac{1}{2}h_{yy}y^2 + \frac{1}{2}(h_{xy} + h_{xyx})xy; \tag{A.3}$$

The surface elevation ,h, is positive if it is above the equilibrium level, and the depth function D is positive bellow the same equilibrium level. Therefore $D + h$ is the total depth of water.

To satisfy the continuity equation the depth function is described by equation A.4:

$$D = D_0(1 - \frac{x^2}{L^2} - \frac{y^2}{l^2}). \tag{A.4}$$

so that the basin is an elliptical paraboloid. The equilibrium shoreline is determined by $D = 0$ and is the ellipse described by equation A.5

$$\frac{x^2}{L^2} + \frac{y^2}{l^2} = 1. \tag{A.5}$$

The time dependent coefficients in equationsA.2, A.3 and A.4, u_0, u_x, u_y, v_0, v_x, v_y and h_0 must vanish in order to satisfy the continuity equation, thus the coefficients described are required to satisfy the following equations:

$$\begin{gathered}
\tfrac{\delta h_0}{\delta t} + (u_x + v_y)(D_0 + h_0) + u_0 h_x + v_0 h_y = 0; \\
\tfrac{\delta h_x}{\delta t} + (2u_x + v_y)h_x + v_x h_y + u_0(h_{xx} - \tfrac{2D_0}{L^2}) + v_0 h_x y = 0; \\
\tfrac{\delta h_y}{\delta t} + (2v_y + u_x)h_y + u_y h_x + v_0(h_{yy} - \tfrac{2D_0}{l^2}) + u_0 h_x y = 0; \\
\tfrac{\delta h_{xx}}{\delta t} + (3u_x + v_y)(h_{xx} - \tfrac{2D_0}{L^2}) + 2v_x h_{xy} = 0; \\
\tfrac{\delta h_{yy}}{\delta t} + (3v_y + u_x)(h_{yy} - \tfrac{2D_0}{l^2}) + 2u_y h_{xy} = 0; \\
\tfrac{\delta h_{xy}}{\delta t} + 2(u_x + v_y)h_{xy} + u_y(h_{xx} - \tfrac{2D_0}{L^2}) + v_x(h_{yy} - \tfrac{2D_0}{l^2}) = 0.
\end{gathered} \tag{A.6}$$

The six equations plus the requirement that $h_{xy} = h_{yx}$ which leads to:

$$\frac{\delta}{\delta t}(v_x - u_y) + (u_x + v_y)(v_x - u_y + f) = 0; \tag{A.7}$$

12 initial conditions total are needed, corresponding to the initial values of u_0, u_x, u_y, v_0, v_x, v_y, h_0, h_x, h_y, $h_x x$, $h_y y$ and $h_x y$, which fully define the initial fields u, v, h.

Appendix B

Compaction of experimental embankments. Control and Execution

B.1 Compaction procedure

1 - Mix the soil to promote homogeneity in the mixture and to break apart lumps of soil and clay;

2 - Remove obvious big rocks from the soil;

3 - Clean the embankment site with water to promote adherence of the first layer of the embankment;

5 - Drop the soil consistently in a single location and then spread, this promotes uniformity of the layer and does not have a compaction action on the soil. Remove any rocks or lumps of clay if there are any;

6 - Layer height = 15 cm;

7 - Switch on the compaction plate;

- switch the ignition button on;
- pull the string to turn the motor on;
- switch off the ignition button;
- Select the frequency of the vibratory plate;

8 - Pass the compaction plate in a straight line along the length of the embankment at a steady; pace(similar to the executed in the test embankments). Avoid stepping on parts of the embankment that have yet to be compacted;

9 - Repeat step 8 until the number of passes has been achieved;

10 - Do the compaction control using a non invasive test after half the embankment design height has been reached.

B.2 Trial embankments

Trial embankments are made to test compaction techniques and equipments, and its results at a small scale and reduced cost, without acting on the design embankment. In the experiments trial embankments where made to draw the compaction curve of the compaction plate by varying the number of passes and keeping the water content in the soi- The trial embankment was composed of 2 layers. The first layer measuring **5 cm** is a retreading layer so the concrete does no influence the compaction technique. The second layer measured **15 cm**, corresponding to the layer height used in the design embankment. The process is demonstrated in figure B.1

a)

b)

c)

d)

Figure B.1: Trial embankment construction process (a) ; b) ; c)) and sand bottle test (d))

Controled variables. Results

The variables monitored using the trial embankments where the number of passes with the compaction plate, the speed of the passing and the frequency of the vibratory plate.

Figure B.2 shows the resulting compaction curves for 1, 3 and 6 passes with the equipment.

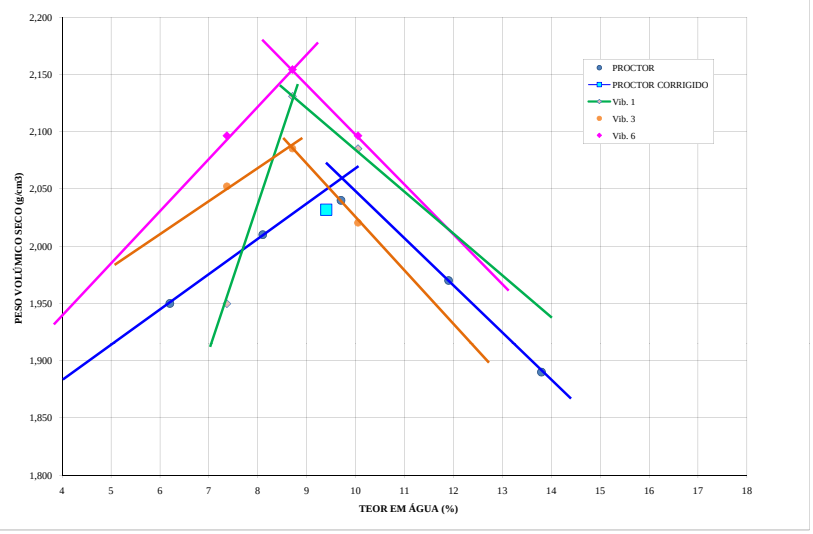

Figure B.2: Grain size distribution curve. Exterior of the soil bank.